Building a random forest machine learning model for ~~carbon budget~~Net Ecosystem Exchange estimation in agricultural fields using discontinuous atmospheric Eddy Covariance measurements.

Camille Pery[1,2,3], Pierre Polsenaere[1], Eric Lamaud[2], Natacha Volto[43], Nathalie Long[43], Jonathan Deborde[1], Shunko Bolsée[2], Olivier Philippine[56], Vona Méléder[64,75], Christine Dupuy[43]

[1] Ifremer, COAST, 17390 La Tremblade, France
[2] INRAe, ISPA, 33140 Villenave D'Ornon, ~~France~~France
[3] Univ. Bordeaux, CNRS, Bordeaux INP, UMR 5805, F-33600 Pessac, France
[43] LIENSs, UMR7266 CNRS- La Rochelle Université, 17000 La Rochelle, ~~France~~France
[5] Unima, 17180 Périgny, France
[64] Nantes Université, ISOMer, 44000 Nantes, France
[75] Institut Universitaire de France, IUF, France
~~[6] Unima, 17180 Périgny, France~~

Correspondence to: Camille Pery (camille.pery@bordeaux-inp.fr)

Abstract. Atmospheric CO_2 exchanges in agroecosystems are strongly controlled by plant phenology, management and microclimatic conditions~~:~~, yet obtaining finely resolved flux estimates across heterogeneous agricultural landscapes remains challenging. This study evaluates the ability of a single Eddy Covariance (EC) system combined with wind-sector partitioning and Random Forest (RF) modelling to estimate ~~annual~~ the ~~carbon budgets~~Net Ecosystem Exchange (NEE) of adjacent fields (wheat, mixed-grain, permanent grassland) in the Marais p~~P~~oitevin wetland (French Atlantic coast). Fluxes were measured over the period 2023-01-01-2024-01-31 and attributed to the different fields by wind sectors. Two modelling strategies were compared (i) a single global RF trained on all sectors and (ii) sector-specific RFs for each adjacent field. RF models globally showed good overall performance ($R^2 \approx 0.2068$-0.945 depending on sector and period), but this apparent equivalence broke down once fluxes were reconstructed over the full annual cycle: the sector-specific approach then better reproduced phenological dynamics and management-driven flux reversals (harvest, grazing) than the global model, which compressed inter-sector variability by up to 67%.~~while the sectoral approach better reproduced phenological dynamics and responses to management events (harvest, grazing) than the global model, which tended to smooth site-specific signals.~~ Annual NEE estimated from the sector-specific models indicate that the mixed-grain field acted as net source (+151 g C m^{-2} yr^{-1}), whereas the permanent grassland and the wheat field acted as net sinks (−145 and −308 g C m^{-2} yr^{-1}). ~~Annual carbon budgets~~NEE ~~estimated from the sectoral models indicate that the permanent grassland and the wheat field acted as net sinks (−259 and −216 g C m^{-2} yr^{-1}, respectively), whereas the mixed grain and the hybrid field behaved as net sources (+182 and +231 g C m^{-2} yr^{-1}).~~ A light-response-curve partitioning of these reconstructed fluxes into gross primary production (GPP) and ecosystem respiration (Reco) revealed contrasting phenological signatures behind different land-cover. Main limitations include spatial attribution uncertainty related to footprint mixing with ditch and riparian vegetation for sectors adjacent to these features, ~~to~~

the EC footprint under stable conditions, flux disturbances during stormy episodes, and the limited one-year observation period. This study highlights the novelty and practical value of coupling a single EC system with wind-sector partitioning and machine learning approaches to resolve carbon fluxes at the field scale within heterogeneous agricultural landscapes. This integrated approach provides a cost-effective alternative to traditional multi-tower setups, offering new opportunities to monitor spatial carbon dynamics and management effects in real agricultural mosaics. Beyond methodological innovation, this work provides one of the first field-scale, uncertainty-resolved carbon flux datasets for a mosaic of contrasting agricultural land covers monitored by a single EC tower, offering a transferable framework to better constrain the terrestrial carbon balance of retro-littoral wetland landscapes.the goal of this work is to establish a comprehensive carbon budgetNEE values not merely for a single agroecosystem, but for the terrestrial component of a wetland area, capturing the complexity of its ecological and biogeochemical interactions.

Keywords: Eddy Covariance, Random Forest, carbon budgetNet Ecosystem Exchange, wind sectors, agriculture, gap-filling.

1 Introduction

Agricultural lands cover a vast fraction of the terrestrial biosphere with around 50% of the Earth's vegetated land surface (about 5 billion ha) under cultivation, grassland or rangeland (Zomer et al., 2017);. tThis extensive area makes agroecosystems as a major component of the global carbon cycle. Indeed, since 1750 corresponding to the start of the industrial era, conversion of forests and meadows to cropland and grassland has released large amounts of CO_2 on the order of 214 ± 67 PgC from biomass and soils, contributing roughly to a quarter of anthropogenic greenhouse-gas emissions (Zomer et al., 2017). In the last decade, net CO_2 emissions from land-use change (mostly driven by agriculture) averaged about 4.2 ± 2.6 Gt CO_2 yr^{-1} (Friedlingstein et al., 2025). At the same time, agricultural ecosystems can remove atmospheric CO_2 through crop photosynthesis and store part of this carbon in plant biomass and soils. However, their overall role as a carbon sink or source depends largely on agricultural management practices too. Conventional practices, such as intensive tillage and crop residue removal, can reduce soil carbon stocks and increase greenhouse gas emissions, whereas more conservational practices, including reduced tillage and crop residue retention, can enhance soil carbon sequestration and mitigate CO_2 emissions. At the same time, crops and managed fields also take up significant amount of carbon from the atmosphere via photosynthesis, so agricultural ecosystems can act as both carbon sinks and sources for theof atmospheric CO_2. For example, intensive agriculture can store carbon in plant biomass and soils, while conventional cropping and elimination of residues can turn fields into net sources of CO_2 due to large soil respiration rates. Globally, agricultural soils hold on the order of 8-10% of the world's soil organic carbon (Wu et al., 2024), so even small changes in land management can have measurable impacts on the atmospheric CO_2 concentration. At the same time, Cclimate and land-use intensity control the Net Ecosystem Exchange (NEE) the CO_2 exchange of agroecosystems in complex and interconnected ways: solar radiation and air temperature are the primary drivers of gross primary production (GPP) in many temperate croplands (Moreaux et al., 2020), while water availability, plant

phenology and vapor pressure deficit (VPD) modulate the growing-season uptake. Crop type and anthropogenic management (e.g. fertilization, irrigation, harvest) further alter the balance between photosynthesis and respiration; for instance, deep-rooted or perennial crops typically achieve higher seasonal carbon uptake than shallow-rooted annuals, and no-harvest practices slow down soil CO_2 release. Thus, the net carbon budget of agricultural fields sensitively depends on crop species, phenological stage, and local environment variables, as well as on socio-economic factors determining land-use intensity (Moreaux et al., 2020; Zomer et al., 2017).

To quantify ~~land-atmosphere CO_2 exchange~~NEE over large spatial scales and fine time resolution, the atmospheric Eddy Covariance (EC) technique has become a widely used method in ecosystem science, although it remains costly and technically demanding. EC deploys fast response anemometers and CO_2/H_2O Infra-Red Gaz Analysers (IRGA) on towers to directly measure the turbulent flux of CO_2 between the biosphere and atmosphere (Baldocchi, 2020). Since the late 1990s, global networks of EC towers (e.g. FLUXNET, AmeriFlux, AsiaFlux, etc.~~etc.~~) have accumulated long time series of carbon and water fluxes from hundreds of sites representing diverse biomes (Baldocchi, 2020). In Europe, the Integrated Carbon Observation System (ICOS) network similarly provides standardized CO_2 flux measurements through 180 stations deployed across 16 European countries. ~~at dozens of sites.~~ In total, these networks ~~(i.e. about 130 stations across all networks, including 19 ecosystem stations in France)~~ have been invaluable for linking ecosystem carbon exchange to climate drivers; they ~~. These networks~~ include sites across continents (North America, Europe, Asia, Africa, etc.) and ecosystem types from boreal and temperate forests to grasslands, croplands, wetlands, and even urban landscapes. For example, Baldocchi (2020) notes that EC networks now span the main climate and ecological spaces, revealing how gross primary production (GPP) and ~~ecosystem~~ ecosystem respiration (R_{eco}) respond to sunlight, temperature and moisture. These multi-decadal observations have elucidated several key environmental controls on ecosystem carbon cycling. Solar radiation emerges as the primary driver of photosynthetic carbon uptake, with light response curves showing saturation effects at high irradiance levels and demonstrating how different vegetation types exhibit varying light-use efficiencies (Reichstein et al., 2007; Wohlfahrt and Gu, 2015). Temperature controls operate through multiple pathways: while moderate warming generally enhances both photosynthesis and respiration, the temperature sensitivity ~~(Q_{10})~~ of respiration, commonly expressed as the Q_{10} coefficient (i.e., the factor by which a biological process increases for a 10 °C rise in temperature), typically exceeds that of photosynthesis, leading to reduced net carbon uptake at higher temperatures (Kirschbaum, 1995; Lloyd and Taylor, 1994; Mahecha et al., 2010). Moisture availability represents another fundamental control, with vapor pressure deficit (VPD) strongly regulating stomatal conductance and thus photosynthetic rates, while soil water content directly affects both plant productivity and microbial respiration (Knauer et al., 2018; Novick et al., 2016).

EC measurements also have well-known limitations; for instance, raw flux time series typically contain gaps due to instrument maintenance, met~~e~~orological conditions (precipitation), low turbulence or filtering of spurious data. Then, filling these gaps is necessary, requiring statistical or machine-learning gap-filling routines, which can at the same time, introduce uncertainty

if large or systematic gaps occur (Gao et al., 2023). Moreover, an EC tower integrates fluxes over an upwind footprint whose size and shape change with surface roughness, atmospheric stability and wind direction; in heterogeneous landscapes, a single tower may sample multiple land covers, complicating attribution of fluxes to specific fields or vegetation types. Such footprint heterogeneity can bias estimates when land cover is patchy, a particular concern for small agricultural fields in a mosaic of crops and fallows (Kumari et al., 2020a; Bou-Zeid et al., 2020).

Recently, Machine Learning (ML) techniques have been increasingly applied to model and gap-fill ~~carbon fluxes~~NEE, taking advantage of large EC datasets and remote-sensing/meteorological inputs. Unlike simple empirical regressions or process-based models that require detailed parameterization, ML methods can capture complex nonlinear interactions without explicit mechanistic assumptions. Typical algorithms include Random Forests (RF), artificial neural networks, support vector machines, and ensemble approaches. For example, Zeng et al. (2020) used a RF model to upscale EC-based ~~net ecosystem exchange (~~NEE~~)~~, ~~gross primary production (~~GPP~~)~~ and ~~community respiration (C~~R_{eco}~~)~~ from FLUXNET datasets across the globe, producing high-resolution carbon flux maps. In agricultural contexts, ML has proven effective for both gap-filling and predictive modelling. Gao et al. (2023) demonstrated that a~~n~~ RF-based gap-filling framework (combined with moving-average decomposition) outperformed conventional methods (including linear interpolation, mean diurnal variation, and look-up table approaches commonly used in the FLUXNET standardized processing) over extended CO_2 flux gaps. A recent study applied a knowledge-guided ML framework to agroecosystems in the U.S. Corn Belt and showed it surpassed both pure process models and "black-box" ML models in quantifying carbon dynamics (Liu et al., 2024). These studies highlight key advantages of ML, i.e., flexibility in assimilating diverse inputs (weather, soil moisture, phenology, management) and the ability to identify subtle patterns in flux variability. In practice, ~~Random Forests~~RF are especially popular for flux prediction because they are robust to overfitting and provide variable importance metrics.

In this context, the La Rochelle Zero Carbon Territory (LRTZC) project (2019-2027) provides a regional framework for carbon monitoring and mitigation in the perimeter of La Rochelle Agglomeration. The project has pledged carbon neutrality by 2040 through combined mitigation and sequestration efforts. Under LRTZC, the Blue Carbon axis and associated research actions target carbon fluxes in coastal ("blue carbon") and retro-littoral ecosystems that correspond to freshwater, brackish and salt shallow systems separated from tidal immersion by dykes and locks, and are now numerous particularly along the French Atlantic coast. As part of these efforts, an ~~Eddy Covariance flux~~EC tower has been established from February 2023 to February 2024 in a rural wetland (freshwater marsh, Marans) to monitor retro-littoral ~~atmospheric CO_2 exchanges~~NEE. This wetland ecosystem is constituted by agricultural parcels (terrestrial compartment) separated by ditches (aquatic compartment). Because the EC system cannot fully isolate fluxes from the water ditches, this single tower overlooks three adjacent fields with different crops and management histories. By partitioning the 360° EC data into specific chosen wind-direction sectors, the "wind-sector approach" adopted in the present study allows analysing separate NEE time series for each parcel of interest depending on wind directions.

The objective of this study was to estimate the ~~carbon budgets~~NEE of the three individual fields using the sector-specific EC data. ~~Random Forest~~RF models were built for each wind sector to predict CO_2 flux from meteorological and soil variables measured at the tower location. Annual NEE was then computed for each parcel. NEE was further partitioned into gross primary production (GPP) and ecosystem respiration (Reco) for each sector, using a light-response-curve approach applied to daytime NEE, in order to quantify the relative contribution of photosynthetic uptake and respiration to each parcel's annual carbon budget. ~~Diurnal flux dynamic was also examined to distinguish photosynthetic uptake from nighttime respiration and thus quantify the contribution of respiration to each parcel's carbon budget.~~ To test the benefit of this disaggregated approach, a "pooled" model was ~~also~~ trained using all data from all sectors (ignoring field boundaries), and its flux predictions ~~and budget~~ were compared to those from the separate specific models. The hypothesis was that sector-specific models would more accurately capture each field's distinct ~~CO_2 exchange~~NEE (reflecting crop and management differences) and thus yield more precise ~~carbon budgets~~values than a single model that pooled all fields. By evaluating disaggregated versus pooled modelling, the study aimed to demonstrate how wind-sector partitioning could enhance carbon monitoring in heterogeneous agricultural landscapes. In this way, complete annual ~~carbon budgets~~NEE values of neighbouring fields could be compared under the same climatic conditions without multiple tower needs.

2 Materials and methods

2.1 Study site

The study was conducted in the city of Marans, located in the Charente-Maritime department in southwestern France (46.31° N, 0.99° W). Charente-Maritime is characterized by a temperate oceanic climate and a predominantly agricultural landscape representing 62% of the total Charente-Maritime region surface, corresponding to 425,267 ha~~agricultural landscape, with 62% of its surface area spent to agricultural use, amounting to 425,267 ha (Agreste, 2020);~~ t~~T~~he regional land use is dominated by cereal crops (63% of the utilised agricultural area, UAA), followed by permanent grasslands (18%), alongside viticulture and livestock farming (Agreste, 2020).

The experimental site comprises three adjacent land parcels representative of the regional land use structure. To the northeast, a parcel was cultivated with mixed grain, sown in autumn and harvested on 24 May 2023, after which the field remained as bare soil for the remainder of the measurement period. To the south, a second parcel was planted with wheat in February and harvested on ~~10~~ 7 July 2023. In the northwest, a permanent grassland parcel, continuously grazed by cattle from June to November (i.e. cattle numbers of 10 in February 2023, 41 in April 2023 and 43 in July 2023), was maintained throughout the study. Each parcel is delineated by hydrological features, including a network of drainage ditches typical of the Marais p~~P~~oitevin wetland system (Butzer, 2002). The Brune Ditch runs between the northern parcels and the wheat parcel and is intersected by a smaller secondary ditch bordered by sparse woody vegetation separating the mixed grain and grassland fields.



Figure 1. Agricultural fields located in the Poitevin Marsh (Marans city) seen by the atmospheric Eddy Covariance station (red dot) deployed from February 2023 to April 2024. Wheat field in the south, mixed-grain field in the northeast and grassland in the

northwest sectors (Drone orthomosaic image taken in February 2023). The Brune Ditch (in brown) orientated from west to east, separates wheat fields in the south from mixed-grain and grassland fields in the north.

The Eddy Covariance (EC) tower was installed on the 1st of February 2023 at a narrow-grassed strip approx. 5 m wide adjacent to the Brune Ditch, providing a central location from which flux measurements could be made across the multiple land covers. The site configuration allowed for the assessment of atmospheric CO_2 fluxes (NEE) across contrasting land uses within a complex agricultural landscape.

2.2 Atmospheric CO_2 exchanges and associated meteorological data measured at the ecosystem scale by Eddy Covariance method

2.2.1 Eddy Covariance data acquisition

The atmospheric ~~Eddy Covariance~~EC technique is a micrometeorological method that quantifies net CO_2 fluxes at the ecosystem-atmosphere interface. In the atmosphere, CO_2 is transported by numerous ~~homogeneous~~ eddies of varying size and frequency. These eddies occur ~~are~~ in the surface boundary layer. ~~This method relies on capturing, within these eddies, the covariance between vertical wind speed (w), air density (ρ), and the dry mole fraction of the gas of interest (s), which can be expressed as:~~ The method relies on measuring the covariance between fluctuations in vertical wind velocity and scalar concentrations within these eddies. The CO_2 flux can be expressed as:

$$F = \overline{\rho\rho_d ws} \approx \overline{\rho_d\rho w's'}$$

where the overbar indicates the time averaging and the prime represents fluctuations around this average (Burba, 2013; Reynolds, 1886). Here, (ρ_d) denotes the dry air density (kg m^{-3}), (w) the vertical wind velocity (m s^{-1}), and (s) the dry mole fraction of CO_2 (mol mol^{-1}, commonly expressed in µmol mol^{-1} or ppm). The covariance between these variables yields a mass flux with units of kg m^{-2} s^{-1}. For CO_2 exchange studies, this mass flux is converted into a molar flux by dividing by the molar mass of CO_2 (MCO_2 = 44.01 g mol^{-1}) and is therefore commonly reported in µmol m^{-2} s^{-1}. Negative CO_2 flux values indicate the ecosystem acts as a CO_2 sink, while positive flux values indicate ecosystem source behaviour.

~~In this study, measured fluxes were averaged every 10 minutes to maximize the number of observations. Negative CO_2 fluxes indicate the ecosystem acts as a CO_2 sink, while positive fluxes indicate ecosystem source behaviour. Fluxes are given in µmol m^{-2} s^{-1}.~~

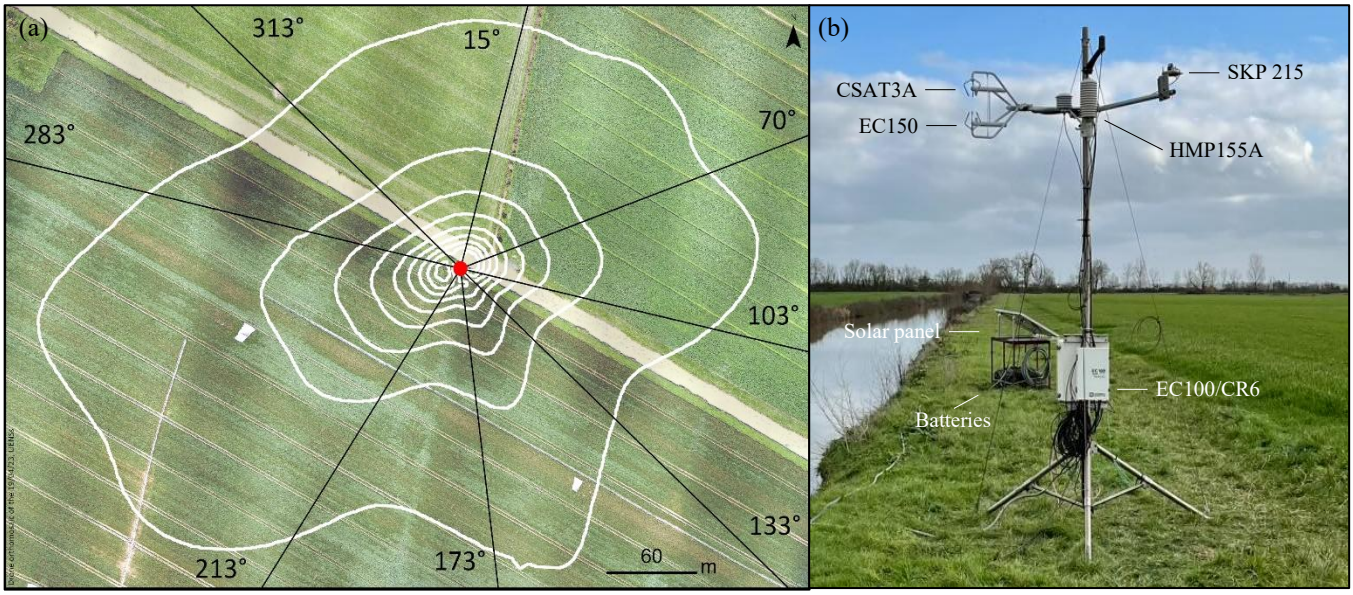


Figure 2. (a) Study site spatial partitioning into wind direction sectors for footprint-based attribution of CO_2 flux measurements to land cover types. High-resolution drone orthomosaic of the study area showing angular sectors centred on the ~~Eddy Covariance (~~EC~~)~~ tower (red dot). 15° to 70°: Sector 1 (hybrid transition zone), 70° to 103°: Sector 2 (mixed grain), 103° to 133°: Sector 3 (ditch), 133° to 283°: Sectors 4, 5 and 6 (wheat), 283° to 313°: Sector 7 (ditch), and 313° to 15°: Sector 8 (grassland).~~15° to 70°: hybrid part of the site, 70° to 103°: mixed grain, 133° to 283° (excluding 173° to 213°, see main text explanations): wheat and 313° to 15°: grassland.~~ 10% to 90% contour lines in white of the annual footprint. (b) The atmospheric EC station set-up with the two main anemometer and CO_2 EC sensors (CSAT3A and EC150, Campbell Sci.) linked to EC100 electronics module connected to the data acquisition central (CR6), with the associated environmental sensors (HMP155A, SKP 215 and TE525MM). The system is powered by batteries charged by solar panels (see main text for more details).

Mean fluxes were calculated over a 10 min. averaging time period we now use since several years, as particularly adapted for more coastal and dynamic systems such as wetlands (present study), salt marshes (i.e., Mayen et al., 2024) and tidal flats (i.e., Polsenaere et al., 2012). For the present study, computations done comparing the friction velocity, wind speed and flux data between the mean of the three 10 min. values and the corresponding mean values obtained with an averaging time period of 30 min. (see graphs in Appendix A, Fig. A1) showed no low frequency losses on the 10 min. flux data, though some dispersion between both 10 min. and 30 min. mean values (u^*, wind speeds, mean fluxes) were noticed. Choosing a 10 min. averaging time period (instead of 30 min.) permitted losing less data due to non-stationary conditions and/or electronical noises leading to potential and more data suppression (with the 30 min. choice) according to our data quality check procedure adopted in the present study (see Appendix A, Fig. A1 and detailed procedure below in Section 2.2.2).

The EC station (Campbellsci), installed and monitored from February, 1st 2023 to April, 3rd 2024 between three~~3~~ agricultural parcels (Fig. 1), includes ~~several key~~the following sensors positioned at the top of a 3m tower mast (Fig. 2b):~~.~~ ~~These sensors~~

~~include~~ an ultrasonic anemometer (CSAT3A) that measures three-dimensional wind speed components, and an open-path IRGA (EC150, connected to the EC100 central) that measures CO_2 and H_2O concentrations in the air both at a frequency of 20 Hz. The ~~tower is~~station also included~~composed of~~ additional sensors measuring various environmental parameters every 10 minutes: a photosynthetically active radiation (PAR) sensor (SKP215), an air temperature and relative humidity sensor (HMP155A), and a rainfall sensor (TE525MM, Texas Electronics) positioned few meters away in front of the tower. Soil temperature and water content were measured by another probe (CS655). The data acquisition system was powered by two batteries (12 volts, 260 Ah) charged by monocrystalline solar panels (24 V, 200Wp module with MPPT 100 V/30 A controller; Victron Energy). High-frequency data were recorded on an SD micro-card and replaced every two weeks along sensor cleaning. Meteorological data were stored in the central acquisition system (CR6 datalogger, Campbellsci) (Fig. 2b).

2.2.2 EC data processing and filtering

Raw EC data were processed using the EddyPro software (EddyPro® v7.0.8, LI-COR Inc.) ~~to ensure accurate CO_2 flux measurements~~. Following Vickers and Mahrt (1997) the processing included several key steps: (1) unit conversion to check that the units for instantaneous data are appropriate and consistent to avoid any errors in the calculation and correction of CO_2 fluxes; (2) despiking to remove outliers in the instantaneous data from the anemometer and gas analyser due to electronic and physical noise and replaced the detected spikes with a linear interpolation of the neighbouring values; (3) amplitude resolution to identify situations in which the signal variance is too low with respect to the instrumental resolution; (4) double coordinate rotation to align the x axis of the anemometer to the current mean streamlines, nullifying the vertical and cross-wind components; (5) time delay removal by detecting discontinuities and time shifts in the signal acquisition from the anemometer and gas analyser (i.e. covariance maximization option for the time lag detection method that calculates the most likely time lag based on the circular correlation procedure to avoid possible flux underestimations in the case of existing potential time lags); (6) detrending with removal of short-term linear trends to suppress the impact of low-frequency air movements; and (7) performing the Webb-Pearman-Leuning (WPL) correction to take into account the effects of temperature and water vapor fluctuations on the measured fluctuations in the CO_2 and H_2O densities (Burba, 2013). Linear detrending was used to calculate fluctuations as the deviations from a linear trend on the chosen 10-minute averaging time period ~~CO_2 fluxes were calculated using the linear detrending method~~ (Gash and Culf, 1996) ~~and averaged over 10-minute intervals~~. Data with more than 10% missing high-frequency data over these 10-minutes were excluded. Then, EddyPro software outputs contains 4% missing values. Additionally, some extreme values in data were identified and removed using the median absolute deviation (MAD) method (Papale et al., 2006). The MAD was calculated over a 2-week window separating daytime and night-time periods. Data above 5.2×MAD were removed. Without extreme values, the number of missing values reaches 12% for the studied period from 2023-02-01 to 2024-01-31. ~~Finally~~In addition, data were filtered removing periods where friction velocity (u_*) values were less than 0.1 m s^{-1}. This parameter quantifies atmospheric turbulence then it allows identifying poorly mixed periods. The EC method often underestimates fluxes during these stable periods due to insufficient turbulent mixing. During these periods, the near-ground air can be decoupled from the air above, leading to an accumulation of CO_2 that is not exactly

captured by measuring instruments (Barr et al., 2013; Gu et al., 2005). This u_* filter optimizes the accuracy of EC measurements particularly during night. After this ~~last~~ filtration the data set contains a total of 32% missing values with 23% of filtered data corresponding to the night, compared with 9% during the day~~.~~ (f~~F~~or more detail, see ~~for instance~~ Mayen et al., ~~(~~2024; ~~) and (~~2025). To go further and remove other extreme values in the dataset particularly during periods of strong meteorological disturbances observed in Autumn 2023 and taking into account crop managements as well, we introduced hard limits based on the observed range of realistic ecosystem fluxes. Before harvest, NEE values were constrained between +20 and −50 µmol m^{-2} s^{-1}, whereas after harvest, when ecosystem activity was substantially reduced, a range of +10 to −10 µmol m^{-2} s^{-1} was applied. These limits removed a small number of spurious observations, including the most extreme values associated with the November storm period in particular (see Appendix A, Fig. A2 and Sect. 2.3 below). After application of this additional hard-limits filter, the overall proportion of missing CO_2 flux data reached 34% for the studied period.

It should be noted that the data-filtering procedure with associated steps~~s~~ described above applies~~y~~ exclusively to CO_2 flux measurements. This filtering does not affect the meteorological variables used as RF predictors, for which the fraction of missing data was minimal (≈0.03% for air and soil temperature and soil humidity, ≈0.005% for relative humidity, and ≈0.68% for wind direction, wind speed and atmospheric pressure), with gaps never exceeding seven consecutive missing values (70 minutes). Given their limited extent and short duration, these gaps were filled using a simple mean-based approach, ensuring temporal continuity of the meteorological inputs without introducing unnecessary complexity.

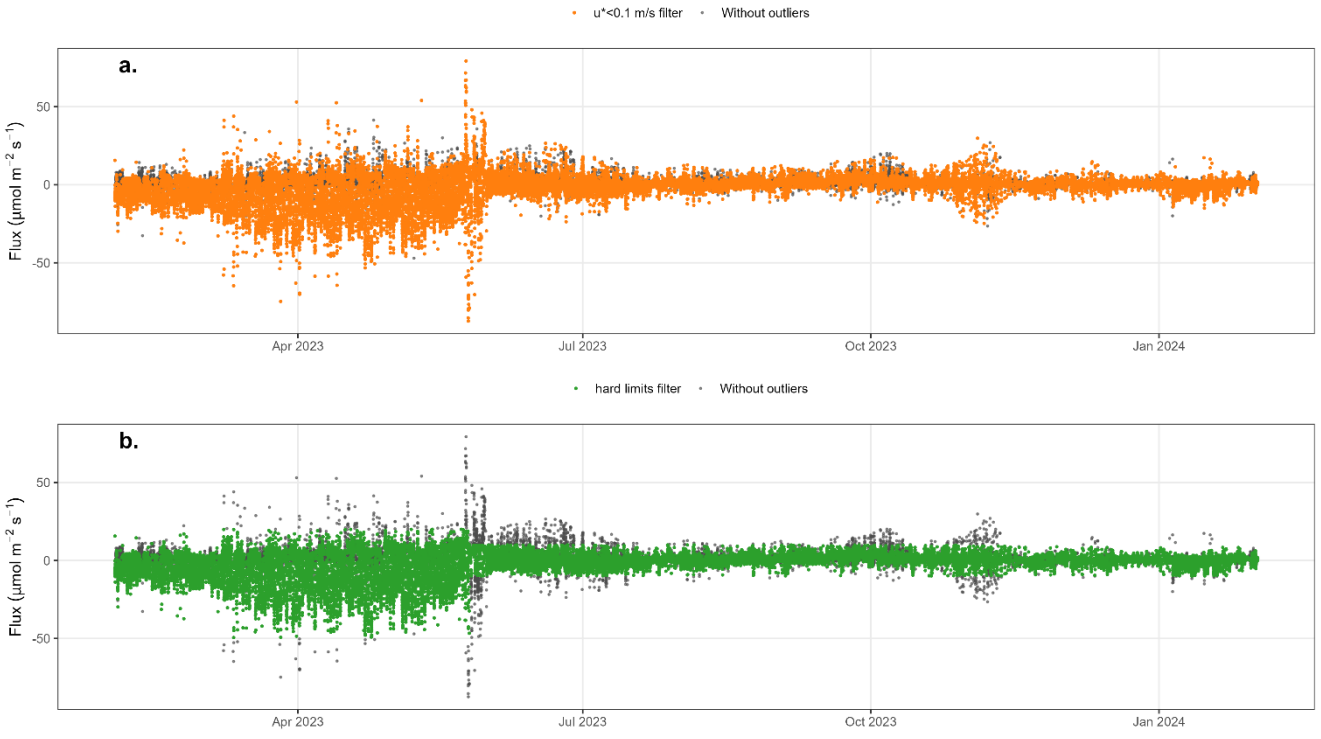


Figure 3. Comparison of ~~Eddy Covariance CO_2 fluxes~~NEE time series after application of (a) the u_* (< 0.1 m s^{-1}) filter and (b) the hard-limits filter. Grey points represent the dataset after outlier removal only, while coloured (orange and green) points indicate the retained fluxes after each filtering step (u_* and hard-limits filter, respectively). Missing data reached 32% after the u_* filter alone and 34.25% after the additional hard-limits filter.

2.3 Intermittent EC data modelling

2.3.1 ~~-~~L~~L~~andscape-based wind sector classification ~~around the EC tower~~, vegetation dynamic analysis and footprint estimation

To spatially constrain the surface sources contributing to the measured ~~CO_2 fluxes~~NEE, we delineated a set of wind sectors that reflect both the surrounding land-cover distribution (Fig. 2a) and the roughness-related flow heterogeneity inferred from turbulence measurements (Fig. ~~4~~3). The objective of the sectorisation was primarily to characterize the spatial heterogeneity of the flux footprint and the effects of contrasting management practices within the study area. In addition to the spatial analysis of landscape structure, we used the ratio between friction velocity (u_*) and mean wind speed (U) as a function of wind direction. Because u_* responds sensitively to upwind vegetation height, discontinuities and surface roughness, directional variations in the u_*/U ratio provide an empirical signature of surface-roughness transitions, making it possible to identify, the position of ditch banks, riparian vegetation or flow disturbances induced by the tower infrastructure (Bolsée et al., 2026). Indeed, in the atmospheric surface layer, the presence of relief elements, whether they are plant-based as in our case or man-made, causes an increase in surface roughness (z_0), which leads to an increase in the roughness coefficient u_*/U, as inferred from the following equation $u(z) = (u_*/k)\ \ln((z - d)/z_0)$. Therefore, the spatial distribution of u_*/U, obtained from momentum EC flux measurements allows differentiating the areas responsible for the CO_2 fluxes measured by the same setup (Bolsée et al., 2026). In the present study, t~~T~~his approach was particularly effective after mowing, when all cropped fields were essentially bare soil while riparian corridors remained vegetated, thereby amplifying roughness contrasts between parcels and allowing a precise alignment between directional u_*/U features and landscape elements. The spatial origin of the measured NEE was determined under all atmospheric stability conditions (instead of selecting only neutral conditions) as it could give a biased view of the sectors where CO_2 fluxes come from, R_{eco} being linked to stable night-time conditions and GPP being the main component of daytime NEE under unstable conditions.

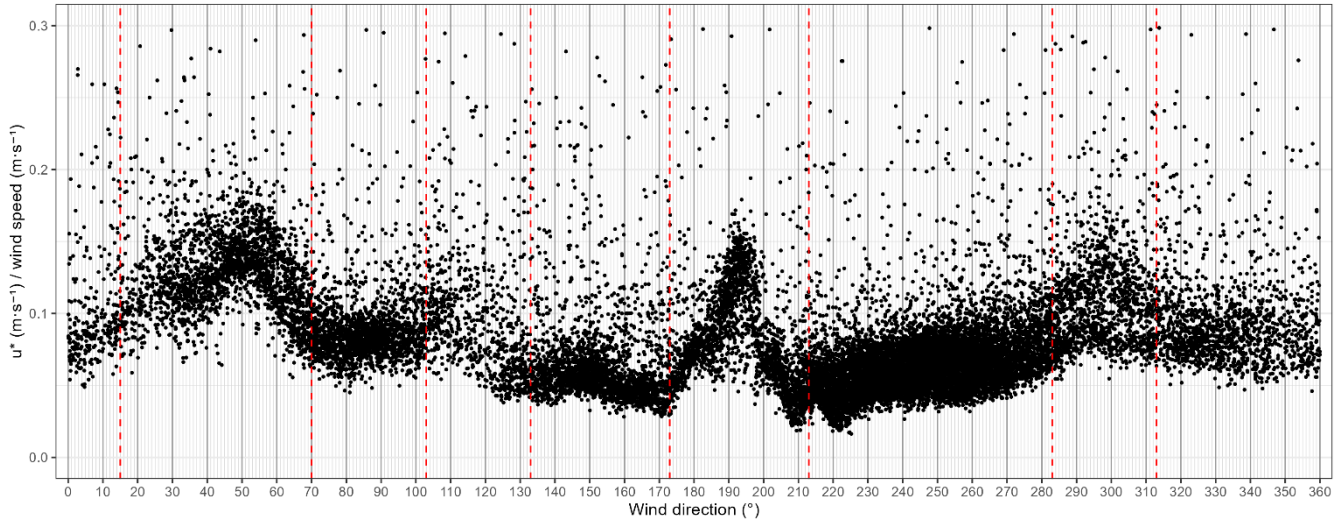


Figure 43. Directional variability of the u*/U ratio after wheat harvest (10/07/2023), highlighting roughness transitions and disturbances used to define wind-sector boundaries (defined by dashed red lines) around the EC tower.

Based on the combined interpretation of land-cover maps and directional u*/U patterns,- the area surrounding the EC tower was partitioned into eight directional sectors reflecting the main land-cover units within the flux footprint (Figs. 2a and 4). Sector 1 (15–70°) corresponds to the transition zone between grassland and mixed-grain parcels, together with the associated riparian vegetation. Sector 2 (70–103°) covers the mixed-grain field, up to the first ditch axis. Sector 3 (103–133°) isolates this first ditch and its bordering riparian corridor. The wheat field, extending from 133° to 283°, was further subdivided into three sub-sectors: Sector 4 (133–173°), Sector 5 (173–213°) and Sector 6 (213–283°), the combination of which (Sectors 4+5+6) reproduces the full wheat sector (133–283°). Sector 7 (283–313°) corresponds to the second part of ditch, centred around ~298°, and its riparian margin. Finally, Sector 8 (313–15°) corresponds to the permanent grassland.~~we redefined the sector boundaries to isolate homogeneous source areas and exclude directions affected by ditches or wake effects. The hybrid sector was set between 15° and 70°, covering the transition zone between grassland and mixed-grain parcels together with associated riparian vegetation. The mixed-grain sector extended from 70° to 103°, up to the first ditch axis, whose influence became evident in the u*/U signal; directions between 103° and 133° were therefore removed to avoid contributions from the riparian corridor bordering the ditch. The wheat field formed a broad upwind domain from 133° to 283°, within which a directional interval (173–213°) was excluded since it corresponds to the sonic anemometer wake, whose peak is clearly visible at 193° (Fig. 3).~~ Sector 5 is centred on the wake of the sonic anemometer, whose peak is visible at 193° (Fig. 4). Although this wake does not directly bias CO_2 fluxes, it locally distorts the wind field in a way that renders the standard u_* filter (< 0.1 m s^{-1}) unreliable within this directional range.

Retaining all eight sectors, was necessary to reduce the imbalance in sample size across sectors and sub-periods: as shown by the associated number of 10-minute observations (Table 1), the eight-sector scheme, together with the pre-/post-harvest temporal split, yields sub-groups ranging from a few hundred to several thousand observations, a spread that a coarser classification would only widen further. In particular, subdividing the wide wheat sector (133–283°) into three narrower sub-sectors (Sectors 4, 5 and 6) allows each of them to be sampled with a comparable, wind-direction-driven density of observations, avoiding a single, very large wheat class from dominating the dataset relative to the smaller mixed-grain, hybrid and ditch sectors (Table 1); this subdivision also makes it possible to assess whether the wheat parcel behaves consistently across its angular extent, or whether spatial heterogeneity remains within a single, apparently homogeneous field. Sectors 3 and 7 (the two ditch/riparian corridors) were retained for a similar diagnostic purpose: rather than providing a stand-alone carbon-flux estimate for the ditches themselves, they serve as a point of comparison for the neighbouring mixed-grain (Sector 2) and grassland (Sector 8) sectors, helping to assess the extent to which riparian and open-water surfaces may contribute to, or "contaminate," the flux signal nominally attributed to these two crop and grassland sectors (see Sect. 3.3, 4.2).

~~cumulative NEEflux Although the wake does not bias CO_2 fluxes directly, it alters u^* in such a way that the standard u^* filter (< 0.1 m s^{-1}) becomes unreliable; removing ±20° around the wake peak ensured the validity of the filtering procedure while preserving a sufficiently large wheat sector dataset. Finally, the second ditch sector (283–313°), centred around the opposite ditch axis (~ 298°), was also excluded using a ±15° margin derived from its roughness signature, for the same reasons as the first ditch interval, namely, to avoid flux contributions from riparian vegetation lining the ditch. The permanent grassland was assigned to the 313–15° sector, covering the pasture area while avoiding adjacent riparian strips. Together, these updated sector boundaries (Figs. 2a and 3) provide a spatially coherent partitioning of the landscape surrounding the EC tower that accounts for surface roughness transitions and ensures that each retained sector corresponds to a homogeneous and well-defined source area for CO_2 flux interpretation. As a result of this sectorization, only 39% of the available flux data were retained for subsequent analyses.~~

~~The Brune ditch sector was not considered due to its narrow width, which prevents obtaining sufficiently representative 10-minute fluxes. The EC technique relies on the averaging of high frequency turbulent fluxes over discrete time intervals (typically 10–30 min). Within such intervals, both wind direction and speed can considerably fluctuate, meaning that the mean wind direction does not strictly correspond to a fixed upwind source area. As a result, each 10-minute flux integrates signals from multiple surfaces whose relative contribution varies with atmospheric stability, turbulence intensity, and surface roughness. Previous footprint analyses have shown that a significant fraction of the measured fluxes (>75% of flux contributions) are generally confined within upwind distances between 15 and 20 times the measurement height, disputing the applicability of the traditional "1:100" fetch-to-height rule under unstable conditions (Kumari et al., 2020). In the present case, this implies that even small fluctuations in wind direction can cause the footprint to intermittently include or exclude the ditch and its riparian margins, preventing any reliable isolation of ditch fluxes within a single directional sector.~~

~~Given its narrow width of approximately 12 m, the Brune ditch represents only a minute fraction of this footprint and cannot generate a dominant or isolable signal within the turbulent flow. Moreover, the ditch is not aligned with the main axis of the EC tower, making it geometrically impossible to define a wind sector that would exclusively sample fluxes from its surface. Any such sector would inevitably include contributions from adjacent vegetation and soil surfaces, especially from the riparian strip bordering the ditch.~~

~~This targeted sector classification enables a more precise attribution of measured CO_2 fluxes to discrete land cover types, while acknowledging the heterogeneity of real-world agricultural mosaics. By isolating homogeneous land parcels and minimizing contamination from unmanaged or mixed areas, this approach improves the interpretability of flux measurements in the context of landscape-scale carbon dynamics.~~

In the present study, the footprint (Fig. 2a) was estimated with the Kljun et al. (2015) model and calculated using the constant measurement height (Zm=3m), the constant displacement height (d = 0.1 m), mean wind velocities, standard deviations of the lateral velocity fluctuations after rotation, the Obukhov length (L), friction velocities (u_*) and wind directions, measured by the station from February, 1st 2023 to 31 January 2024~~April, 3rd 2024~~. No further specific parametrization like aerodynamic canopy height for instance (Chu et al., 2018) was done since averaged footprint we present was sufficient to our modelling approach. Footprint model distance outputs using Kljun et al. (2004) and Kormann and Meixner (2001) footprint models given by EddyPro, were also checked to help estimate whether the ditch's contribution was negligible or not.

NDVI time series were derived from 26 MODIS MOD13Q1.061 Vegetation Indices 16-Day composite products (Terra platform, 250 m spatial resolution, tile h17v04), covering the period from 1 January 2023 to 31 January 2024 and obtained from the NASA Land Processes Distributed Active Archive Center (LP DAAC) via the NASA Earthdata Search portal. To analyse and better understand vegetation dynamics according to phenology and agricultural management, three well-defined "pure" agricultural parcels were delineated, and for each of them, a single NDVI value per date was computed as the spatial mean of all MODIS pixels falling within the corresponding polygon, thereby representing the vegetation status of the parcel as a whole. Riparian vegetation located along the two canals as part of the EC footprint in certain sectors was explicitly excluded from the NDVI-based analysis.~~To analyse and better understand vegetation dynamics according phenology and agricultural management, NDVI time series were computed on well-defined "pure" agricultural parcels only (see Figure 1, showing the three polygon delineations). Riparian vegetation located along the two canals as part of the EC footprint in certain sectors was explicitly excluded from the NDVI-based analysis.~~

2.3.2 Modelling Scenarios and Sector-Specific Approach

To complete and fully characterize the spatio-temporal dynamics of ~~the Net Ecosystem Exchange (NEE)~~NEE measured by EC over the February 2023 - February 2024 period across the study site, ~~Random Forest (~~RF~~)~~ models were implemented according to two distinct strategies. ~~In~~ T~~t~~he first strategy (~~,~~Scenario 1)~~,~~ involved training a single global RF model using pooled data from all sectors (0–360°), representing the standard approach when sector information is not exploited; this global model served as a baseline against which the added value of the sector-specific strategy could be quantified, both in terms of point-prediction performance and reconstructed annual cumulative NEE (Sect. 3.2). ~~This global model was intended to serve as a baseline for comparison, assessing whether joint modelling could match or outperform sector-specific models.~~

In the second strategy~~parallel, an alternative approach~~ (Scenario 2), separate RF models were trained for each landscape-based wind sector classification area and key temporal subdivision, accounting for phenological shifts such as crop harvest for instance that influence flux dynamics over the wheat and mixed-grained areas. Specifically, for each crop parcel, pre- and post-harvest periods were modelled independently to better capture ecosystem transitions, resulting in seven sector-specific models overall (Table 1). Both strategies used the same explanatory variables described in Sect~~ion~~ 2.3.3 to ensure comparability and comparison.

Table 1. Sector definition and temporal subdivision associated with the number of observations recorded each 10 minute~~s~~ from 01/02/2023 to 31/01/2024.

Sector	Land cover	Wind direction range (°)	Temporal split	Split criterion	Model ID	Number of observations	Percentage of gap-filled data
1	Hybrid (grassland/mixed grain transition)	15-70	Yes	24 May	Sector 1 - before Sector 1 - after	2981 3273	88%
2	Mixed grain	70-103	Yes	24 May	Sector 2 - before Sector 2 - after	1130 2307	94%
3	Ditch	103-133	No	-		1207	98%
4	Wheat	133-173	Yes	7 July	Sector 4 - before Sector 4 - after	625 1914	95%
5	Wheat	173-213	Yes	7 July	Sector 5 - before Sector 5 - after	1031 1563	95%
6	Wheat	213-283	Yes	7 July	Sector 6 - before	4931	76%

					Sector 6 - after	7940	
7	Ditch	283-313	No	-		2207	96%
8	Grassland	313-15	No	-		3729	93%
4+5+6	Wheat (combined)	133-283	Yes	7 July	Sector 4+5+6 - before Sector 4+5+6 - after	6587 11417	66%

~~**Table 1. Number of observations recorded each 10 minutes from 01/02/2023 to 31/01/2024 for each selected land cover type (see Fig. 2 and main text for details) and percentage of observations relative to the total number of measurements over the entire year in parentheses. Before and after representing pre- and post- harvest measurements. Harvesting occurred on May 24 for mixed grain and on July 7 for wheat.**~~

~~Hybrid~~		~~Mixed grain~~		~~Wheat~~		~~Grassland~~
~~Before~~	~~After~~	~~Before~~	~~After~~	~~Before~~	~~After~~	
~~2380 (4%)~~	~~2101 (4%)~~	~~832 (2%)~~	~~1533 (3%)~~	~~4685 (9%)~~	~~6666 (13%)~~	~~2192 (4%)~~

~~We thank the Referee for this important clarification request. We agree that the treatment of meteorological data is relevant for the RF parametrization and we provide additional details below. It is important to note the data filtering procedures described in the manuscript apply only to CO_2 flux measurements. As a result, the reported 32% of missing data concerns flux data exclusively and does not affect the meteorological drivers used in the random forest models.~~

~~Regarding meteorological variables, a very small fraction of missing data remained after processed Eddy Pro output: approximately 0.03% for air temperature, soil temperature, and soil humidity, 0.005% for relative humidity, and 0.68% for wind direction, wind speed, and atmospheric pressure. These gaps were generally short, with a maximum duration of 7 consecutive missing values (i.e., 70 minutes).~~

~~Given the very limited extent and short duration of these gaps, we applied a simple mean-based gap-filling approach to ensure temporal continuity of the meteorological drivers used in the Random Forest models. This choice was made to avoid introducing unnecessary complexity while preserving the physical consistency of the predictors.~~

2.3.3 Selection variables for Random Forest modelling

Although variable selection procedures such as Variable Selection Using Random Forest (VSURF) (Genuer et al., 2010) are commonly used to reduce dimensionality prior to ~~Random Forest~~RF modelling, we did not apply automated selection in the present~~is~~ study. Instead, we opted for a targeted set of explanatory variables a priori chosen based on their established

mechanistic links with CO_2 fluxes and their relevance in surface-atmosphere exchange studies. All models were therefore trained using the same set of predictors: photosynthetically active radiation (PAR), day of year (DOY), a qualitative day-night indicator, relative air humidity, soil moisture, soil temperature, wind direction, and air temperature. PAR directly regulates photosynthetic activity and light-driven variations in ecosystem CO_2 uptake; DOY captures seasonal changes in vegetation state and radiation ~~regime; ther~~regime. The qualitative day-night indicator distinguishes periods of daytime and nighttime activity by assigning "day" to time steps with PAR > 10 µmol m^{-2} s^{-1} and "night" to those with PAR ≤ 10 µmol m^{-2} s^{-1}~~day-night indicator separates radiative and non-radiative control periods~~, ~~which~~ and exhibit in turn contrasting drivers of respiration and assimilation. Relative humidity and air temperature influence stomatal conductance and microbial respiration, while soil moisture and soil temperature jointly modulate below-ground respiration and substrate availability. Wind direction was included to account for directional heterogeneity in source areas. ~~Importances~~The importance of these variables chosen and checked for each model are provided in the Appendix B (see Sect. 2.3.4 below and Figs. B2, B3)~~A~~.~~.~~ Explicit seasonal or monthly cyclical time variables though useful in some modelling contexts (Vekuri et al., 2023), were not included here since the main temporal dynamics were already well captured by PAR, DOY and the day/night indicator, and would therefore provide largely redundant information. Moreover, the objective was to keep the model as simple and interpretable as possible, especially since RF models are already able to handle non-linear temporal patterns without requiring explicit seasonal transformations. Similarly, NDVI observations (Sect. 2.3.1) could not be directly used as predictors in the RF model, which was trained on footprint-integrated flux measurements rather than pure-field vegetation indices. At the end, t~~T~~his expert-driven approach ensured that all major biophysical drivers of ~~CO_2 exchange~~NEE were represented while maintaining comparability across sectors and modelling exercises.

It should also be clarified how wind direction, one of the meteorological predictors, was assigned when reconstructing a continuous NEE time series for each sector. All meteorological variables come from the same single EC tower, whatever the wind direction. Each sector-specific RF model was trained and evaluated only on the time steps when the wind actually blew from within that sector's own angular range. To reconstruct NEE continuously for a sector, however, predictions were also needed for time steps when the wind blew from elsewhere, and the RF model still required a wind-direction value as input to produce a prediction. For these time steps, a wind-direction value was drawn at random from within the sector's angular range, while all other meteorological variables (PAR, air and soil temperature, humidity, etc.) were taken directly from the actual tower measurements at that time step.

2.3.4 Model training, performance evaluation and uncertainty quantification

~~To ensure rigorous model optimization and performance evaluation, a systematic approach was implemented. The Random Forest hyperparameter optimization specifically focused on tuning the number of predictors sampled for splitting at each node (mtry), while the number of trees (ntree) was fixed at 400 based on preliminary analyses showing performance stabilization beyond this threshold (Breiman, 2001). The mtry parameter was optimized using a sequential grid search approach, testing~~

~~values from 1 to the total number of selected predictors. For each mtry value, a Random Forest model was trained on the selected variables, and the out-of-bag (OOB) error from the final tree (ntree = 400) was recorded as the performance metric. The optimal mtry value was selected as the one yielding the lowest OOB error.~~

~~Once optimized, model performance was robustly evaluated for both modelling scenarios. In Scenario 1, the global model was trained using the optimal mtry value and evaluated independently for each sector by computing Bias, RMSE, and R^2 metrics on sector-specific subsets of the data. In Scenario 2, separate sector-specific models underwent their own mtry optimization following the same protocol, with each sector's optimal mtry determined independently based on minimizing OOB error.~~

~~This streamlined optimization approach leveraged the inherent cross-validation properties of Random Forest's OOB error estimation, eliminating the need for additional train/test splitting while ensuring robust hyperparameter selection. Finally, each model (global or sector-specific) was trained on the full corresponding dataset using the optimal mtry and ntree = 400 before being used for final CO_2 flux predictions. This evaluation framework maintained consistency while allowing direct comparison between sector-specific and global modelling strategies.~~

Two complementary modelling scenarios were implemented to reconstruct ~~CO_2 fluxes~~NEE values across the different wind sectors. In the first scenario (global model), a single Random Forest (RF) model was trained on the entire dataset, pooling observations across all wind directions (0–360°) without any sector- or period-specific stratification. In the second scenario (sector-specific models), independent RF models were trained separately for each land-cover sector, and, where relevant, for each sub-period defined by a phenological or management transition (e.g., harvest date; Tables 1 and ~~B~~A1), using only the data associated with wind directions falling within the corresponding sector's angular range.

Both scenarios shared an identical RF parameterization. The number of trees was fixed at ntree = 300, consistent with previous evidence that RF performance stabilizes well below this threshold (Breiman, 2001), and the number of predictors sampled at each split (mtry) followed the standard heuristic for regression trees, mtry = $\lfloor\sqrt{p}\rfloor$, where p is the number of candidate predictors (~~photosynthetically active radiation~~PAR, air temperature, relative humidity, wind direction, day of year, soil temperature, soil moisture content, and a day/night indicator; p = 8, yielding mtry = 2).

Uncertainty was quantified identically for both scenarios too, using a bootstrap resampling procedure as providing a more robust basis for evaluating differences among vegetation types and modelling approaches, particularly during disturbance and post-harvest periods when fluxes are highly variable and non-stationary. For each retained model, B = 100 RF models were trained on independent bootstrap resamples of the corresponding training dataset (sampling with replacement, resample size equal to the original dataset size), using the same ntree and mtry values throughout. The resulting ensemble of 100 bootstrap models was used to generate, for each time step, a distribution of predicted CO_2 fluxes: the median of this distribution was retained as the point estimate, and its 2.5th and 97.5th percentiles defined an empirical 95% prediction interval. Model performance (RMSE, MAE, R^2) was assessed using out-of-bag (OOB) predictions: for each observation, predictions were derived only from the subset of trees, within the ntree = 300 trees of each RF model, for which that observation had not been

included in the corresponding internal bootstrap training sample, following the standard OOB procedure inherent to the Random Forest algorithm (Breiman, 2001). This OOB evaluation was applied consistently across the B = 100 bootstrap-resampled models of each scenario, providing an internal, unbiased estimate of predictive performance for both the global and sector-specific strategies, and forming the basis of the OOB validation framework used to compare the two strategies in Sect. 3.2 (Table 2).

For flux reconstruction, continuous predictions were generated separately for each wind sector, using only the wind-direction range corresponding to that sector; whenever the observed wind direction fell outside this range, wind direction was randomly resampled within the sector's angular boundaries to preserve a consistent input space, while all other meteorological predictors were retained from the tower measurements. In the sector-specific scenario, each sector was predicted using its own dedicated bootstrap-ensemble model (and, where applicable, the model corresponding to the relevant sub-period). In the global-model scenario, the same bootstrap-ensemble model, trained on the pooled 0–360° dataset, was applied uniformly to generate predictions for every sector. This design allowed~~s~~ a direct comparison between sector-specific and global reconstructions of CO_2 fluxes, together with their associated uncertainty, across the different wind sectors.

2.4 NEE flux partitioning

~~Annual carbon budgetsNEE were estimated for each parcel using the predicted CO_2 fluxes from both the global and crop-specific models. Predictions were made at 10-minute intervals and expressed in μmol CO_2 m^{-2} s^{-1}. Cumulative annual fluxes were obtained by summing all predicted values for each parcel and converting the total to grams of carbon per square meter per year (gC m^{-2} yr^{-1}) using a factor of 0.0072.~~

~~To distinguish carbon balance components, fluxes were separated into daytime and nighttime subsets. Daytime period (NEE_{day}) EC data were assumed to reflect gross primary production (GPP) though no Kowalski et al. (2003) partition was attempted due to wind direction change with different corresponding habitats seen by the EC tower during each day; nighttime fluxes (NEE_{night}) were attributed to ecosystem respiration (Reco). Separate cumulative sums were computed for each period, enabling quantification of both photosynthetic uptake (NEE_{day}) and respiratory release (NEE_{night}).~~

~~These partitioning estimates provided a more detailed understanding of metabolic fluxes and processes, allowing for the decomposition of net annual balances into their physiological components. The outputs also enabled a direct comparison between the two modelling strategies, assessing the consistency of carbon budget estimations across different levels of model complexity.~~

Net Ecosystem Exchange (NEE) reconstructed by the sector-specific RF models (Sect. 2.3.4) was further partitioned into Gross Primary Production (GPP) and Ecosystem Respiration (Reco) for each sector and for the combined wheat sector (Sectors

4+5+6). Following Kowalski et al. (2003, 2004), daytime NEE (NEEd) can be expressed as a curvilinear (rectangular hyperbolic) function of the incident photosynthetic photon flux density (PAR):

$$NEEd = \frac{a1 - PAR}{(a2 + PAR) - Reco}$$

where a1 is the maximum photosynthetic uptake rate at light saturation (µmol m^{-2} s^{-1}), a2 is the PAR value at which photosynthetic uptake reaches half of a1 (µmol m^{-2} s^{-1}), and Reco is the mean ecosystem respiration rate (µmol m^{-2} s^{-1}) over the time window used to fit the relationship. In the present study, the three parameters (a1, a2, Reco) were estimated by non-linear least-squares regression of daytime NEE (PAR > 10 µmol m^{-2} s^{-1}, following the day/night indicator defined in Sect. 2.3.3) against PAR, applied independently at a daily scale for each sector-specific RF reconstruction. This daily-resolution fitting allows Reco, a1 and a2 to vary from day to day, thereby capturing short-term changes in photosynthetic capacity and respiration associated with phenological development, senescence, harvest and other management events, rather than assuming stationary parameters over longer periods. For each day and sector, Reco obtained from the fit was taken as the estimate of ecosystem respiration for that day (assumed constant over the 24 h cycle), and daily GPP was then derived as the residual between the reconstructed daily NEE and the fitted Re: GPP = NEE − Reco (with GPP negative, by convention, indicating net carbon uptake by vegetation, consistent with the sign convention adopted in Sect. 2.2.1). Daily Reco and GPP estimates were then summed to obtain cumulative annual Reco and GPP for each sector (Sect. 3.4, Table 3, Fig. 9).

3 Results

3.1 Site conditions, measured fluxNEE dnamicsdynamic and phenology of the studied land parcels

Over the full monitoring period (1 February 2023 – 31 January 2024), the Eddy Covariance (EC) system recorded continuous atmospheric CO_2 exchanges together with the associated meteorological and soil variables (Fig. 5). Net Ecosystem Exchange (NEE) followed a clear seasonal pattern, with thestudied site behaving predominantly as a carbon sink from February to the end of May, reflecting the progressive development of crop and grassland canopies under increasing photosynthetically active radiation (PAR) and air temperature values (Figs. 5a, b, d). A pronounced minimum in NEE (i.e. maximum net uptake) occurred around mid-May, coinciding with peak vegetative development across the three underlying land uses (wheat, grassland, mixed grain, Fig. 6). From mid-May onward, NEE values progressively shifted toward a source behaviour, associated with crop senescence, harvest managed operations and increasing soil respiration under warmer, drier conditions (Fig. 5c–g), before stabilising into a moderate source regime during autumn and winter. A distinct disturbance was recorded

in November 2023, when an intense storm produced a sharp rainfall peak and an abrupt increase in soil moisture (Fig. 5a, 5e, f; red box), coinciding with large-amplitude, high-frequency fluctuations in the measured ~~CO_2 flux~~NEE (see Sect. 2.2.2 and Appendix A, Fig. A2)~~see sion~~. Wind direction (Fig. 5h) confirmed that the tower sampled all eight defined sectors (Table 1) over the year, although unevenly, consistent ~~with~~according to the prevailing wind regime at the site.

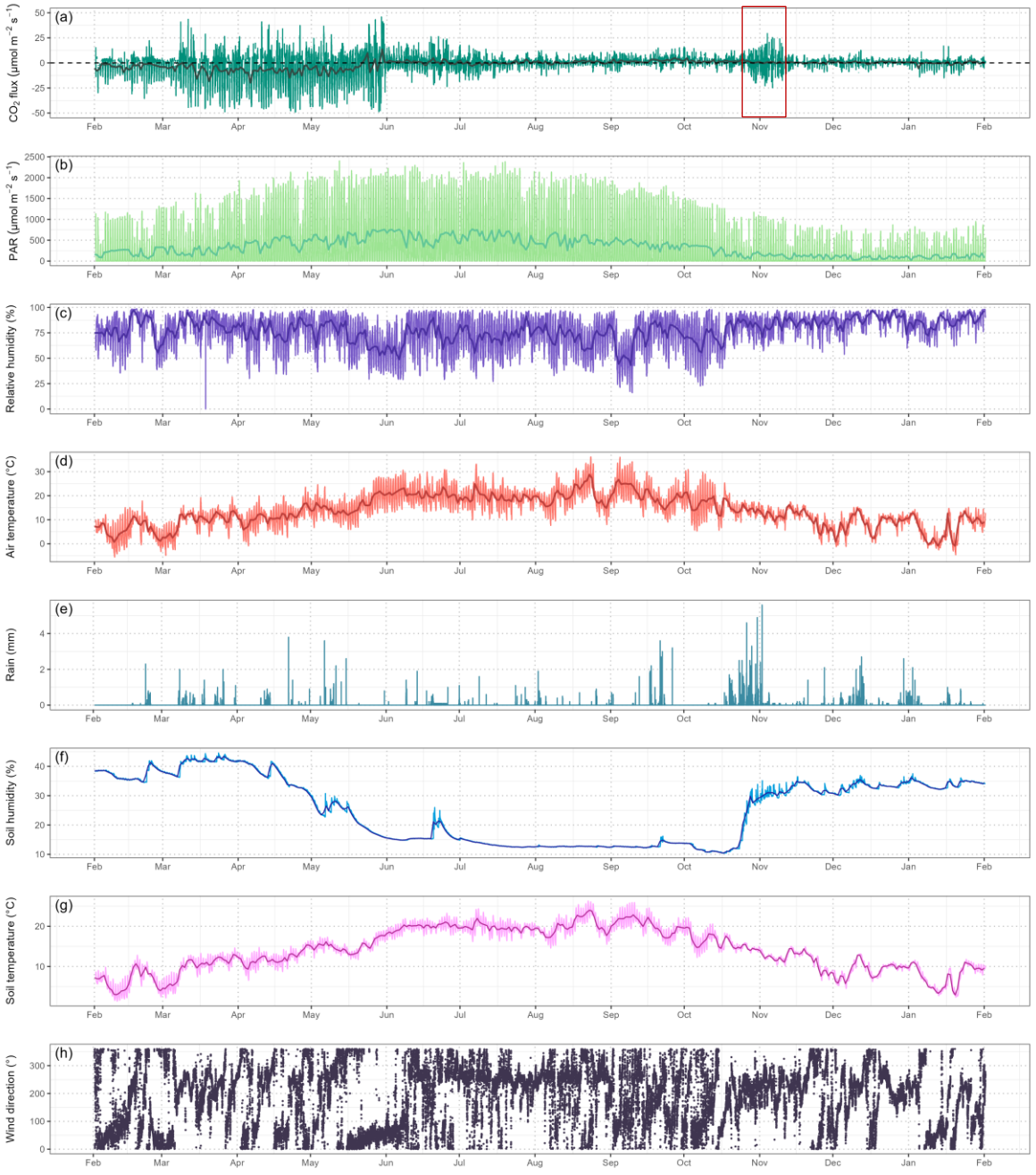


Figure 54. Atmospheric Eddy Covariance measured time series from 01 February 2023 to 31 January 2024 of (a.) atmospheric CO_2 exchanges NEE, (b.) Photosynthetically Active Radiation (PAR), (c.) relative humidity, (d.) air temperature, (e.) rain, (f.) soil humidity, (g.) soil temperature and (h.) wind direction. For CO_2 fluxes, PAR, relative humidity, air temperature, soil humidity and soil temperature, the continuous line represents the daily average obtained from the 10 min values. ~~Box in red represents November's storm.~~ CO_2 flux ~~valueses~~ shown ~~in this figure~~in Fig. 5 correspond to ~~the raw Eddy Covariance~~EC data without hard limits method filtering ~~and areas~~ presented for illustrative purposes only. ~~They were not used for the modelling analyses, as they have not yet been filtered using the hard limits method.~~ The red box highlights the November storm period.

The Sentinel-2 NDVI time series (Fig. 6) illustrated contrasting phenological trajectories among the three underlying land uses. Both the wheat and mixed-grain parcels showed a steady NDVI increase from late winter, reaching maximum canopy greenness in spring. The mixed-grain parcel exhibited an abrupt NDVI decline following its harvest on 24th -May 2023, after which the field remained largely bare until autumn re-sowing that produced a renewed NDVI increase. The wheat parcel maintained high NDVI values later into the season, consistent with its later phenological cycle, and showed a comparatively smaller NDVI discontinuity at harvest because the crop was already senescent and dry at that stage. The permanent grassland parcel displayed the smallest seasonal amplitude, with NDVI values remaining moderate and relatively stable year-round, consistent with continuous grazing and the absence of a single, abrupt senescence event. One can notice that t~~T~~hese independent phenological trajectories, derived from well-defined "pure" parcel polygons that exclude riparian vegetation (Sect. 2.3.2~~3~~), provide an external, remote-sensing-based validation of the crop calendars used to define the pre-/post-harvest temporal subdivisions of the sector-specific models (Table 1).

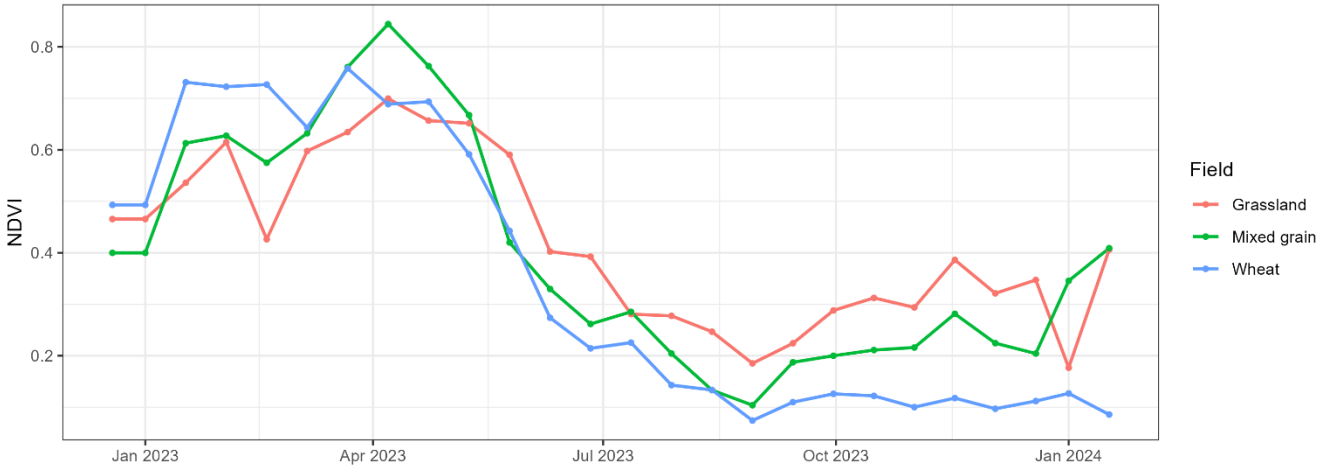


Figure 6. Temporal evolution of MODIS-derived NDVI for the three study fields from January 2023 to January 2024.

~~Performance of the global and sector-specific Random Forest models~~

3.2 Global versus sector-specific RF modelling: point performance and annual flux reconstruction

~~To assess the predictive accuracy of the Random Forest (RF) approach for the different agricultural land covers monitored at the studied site, two modelling strategies were evaluated, a global model trained on the entire dataset, taking vegetation type into account only through a qualitative variable (Scenario 1), and crop-specific models trained independently for each land cover type (Scenario 2).~~

~~For all land cover types, performance differences between the global and crop-specific models were minimal (Fig. 5 and 6). For most crops, R^2 values were almost identical between both scenarios and consistently high, indicating robust predictive performance whatever the modelling strategy. For example, for permanent grassland, both models achieved an R^2 of 0.86. Similarly, in pre-harvest hybrid crop plots, R^2 values were 0.92. RMSE and bias measurements followed the same trend, with only marginal differences between both approaches. However, a notable exception was observed for post-harvest wheat plots. In both modelling scenarios, predictive performance dropped, with R^2 values at 0.44 for both scenarios. This reduced accuracy may reflect greater complexity or noise in the post-harvest flux signals, potentially due to signal disruption from the November storm which introduced a strong rainfall event (visible in Figure 4e) and field inundation during several days as observed at this period; in turn it likely generated artificial flux variations not linked to actual plant or soil activity. Another consistent observation in both scenarios was a greater dispersion of prediction errors for wheat plots, both pre- and post-harvest. In the scatter plots, these plots showed greater variance and a tendency to deviate from the 1:1 line, particularly under low flux conditionsat small flux values. This suggests either a higher degree of temporal variability, or unmodeled management practices or events affecting flux behaviour in wheat systems (Fig. 5 and 6).~~

~~These limitations are particularly important in the context of sparse measurement periods. For instance, during the spring drought observed in May 2023 (Figure 4c, low humidity, figure 4d, high temperature and figure 4e, low rainfall) which coincided with the mowing period, the lack of available data made it challenging to constrain the model. However, the crop-specific models reproduced the water limitation effect more accurately for wheat and grassland than the global RF model (see Section 3.2), even though these parcels were not harvested during that period.~~

The two modelling strategies (Scenario 1, global; Scenario 2, sector-specific) were first compared in an out-of-bag (OOB) validation framework, in which both models were evaluated on exactly the same observations for each of the 13 sector × period sub-groups (n = 34,838 in total; Table 2). Point-prediction performance was overall very similar between the two strategies: R^2 differed by less than 0.02–0.03 and RMSE by less than 5% for most sub-groups (Table 2). The global model nonetheless showed a systematically narrower 95% confidence interval (IC95) than the corresponding sector-specific model in every sub-group, with a reduction of 5 to 16% depending on the sub-group, reflecting the much larger effective bootstrap training sample available to the global model ($n \approx 34{,}800$ vs. 600–8,000 for individual sector-specific models). The sign of the point-

performance difference between strategies depended on sub-group sample size: for the most heavily sampled sub-groups (n > ~3000; e.g. Sector 6-after, Sector 8, Sector 1-after), the sector-specific model matched or marginally outperformed the global model, whereas for smaller sub-groups, the global model showed a modest advantage (e.g. R^2 + 0.06 for Sector 2-after and + 0.07 for Sector 4-after relative to the sector-specific model). R^2 varied widely among sub-groups (0.20–0.94; Table 2), but this range was driven primarily by differences in the amplitude of observed flux variability rather than by absolute model error, which remained comparatively stable across sub-groups (RMSE ≈ 1.5–2.6 µmol m^{-2} s^{-1} for the more stable post-harvest periods and ≈ 3–4.6 µmol m^{-2} s^{-1} for the higher-variability pre-harvest periods).

Table 2. Out-of-bag (OOB) performance of the sector-specific and global RF models for each of the 13 sector × period sub-groups, evaluated on the same held-out observations (n, sample size; Mean and SD, mean and standard deviation of observed flux, µmol m^{-2} s^{-1}; RMSE, root-mean-square error, µmol m^{-2} s^{-1}; IC95, width of the bootstrap 95% confidence interval, µmol m^{-2} s^{-1}).

Model ID	Observations			RMSE sector	RMSE global	R^2 sector	R^2 global	IC width sector	IC width global
	Number	Mean	Sd						
Sector 1 - before	2981	-5.12	10.75	2.98	2.97	0.92	0.92	2.71	2.53
Sector 1 - after	3273	0.97	4.7	2.05	2.09	0.81	0.81	1.66	1.55
Sector 2 - before	1130	-5.99	9.46	2.35	2.24	0.94	0.94	2.41	2.23
Sector 2 - after	2307	0.73	3.11	1.79	1.63	0.67	0.73	1.5	1.4
Sector 3	1207	-1.24	5.64	2.61	2.48	0.79	0.81	2.39	2.09
Sector 4 - before	625	-5.10	11.37	3.73	3.46	0.89	0.91	3.81	3.21
Sector 4 - after	1914	1.20	2.02	1.57	1.53	0.39	0.43	1.30	1.24
Sector 5 - before	1031	-5.14	10.79	4.63	4.56	0.82	0.82	4.12	3.64
Sector 5 - after	1563	0.95	2.18	1.95	1.96	0.20	0.20	1.63	1.42
Sector 6 - before	4931	-6.04	13.54	4.10	4.11	0.91	0.91	3.26	3.10
Sector 6 - after	7940	0.84	2.35	1.62	1.63	0.53	0.52	1.28	1.21
Sector 7	2207	-0.93	5.59	2.38	2.26	0.82	0.84	1.90	1.69
Sector 8	3729	-0.59	7.03	2.24	2.30	0.90	0.89	1.80	1.74

This apparent equivalence between the two strategies did not hold, however, once fluxes were reconstructed continuously over the full annual cycle for each sector (i.e. annual cumulative NEE, Fig. 7). Both strategies reproduced the same qualitative seasonal pattern (a growing sink from February to late May, a marked minimum around June, and a progressive return to source behaviour in late summer/autumn), but diverged markedly in amplitude and relative sector ranking. Under the sector-specific strategy, annual cumulative NEE values ranged from +259 gC m^{-2} (Sector 1, Hybrid) to −370 gC m^{-2} (Sector 6, Wheat), with an inter-sector range of 629 gC m^{-2}. Under the global strategy, the same sectors ranged from +164 gC m^{-2} (Sector 1) to −227 gC m^{-2} (Sector 7), a range of 391 gC m^{-2}, corresponding to an overall compression of about 38% in the amplitude of inter-sector variability (Fig. 7). This compression was uneven across sectors: comparatively small for Sector 8 (grassland, −15%) and Sector 6 (wheat, the best-sampled sector, −45%), but much stronger for Sector 4 (−70%), Sector 5 (−61%) and

Sector 2 (mixed grain, −59%) (the less-sampled sub-sectors). Sector 7 (Ditch East) was a clear exception: rather than being compressed, its cumulative NEE value was amplified under the global strategy (−187 to −227 gC m^{-2}), to the point of inverting its ranking relative to Sector 6 between the two strategies. Taken together, these results show that the global and sector-specific models, despite near-equivalent OOB point performance, yield substantially different spatial pictures of the site's NEE values cumulated (extrapolated) over the full annual cycle for each sector. Because the present site combines strong sub-field heterogeneity in land cover, phenology and management, and because the objective of this study was precisely to resolve field-scale NEE contrasts, the global model was not retained for the remainder of the analysis: all results and interpretations presented hereafter (Sects. 3.3–3.4) are then based on the sector-specific (Scenario 2) reconstructions (see Sect. 4.1 for further discussion).

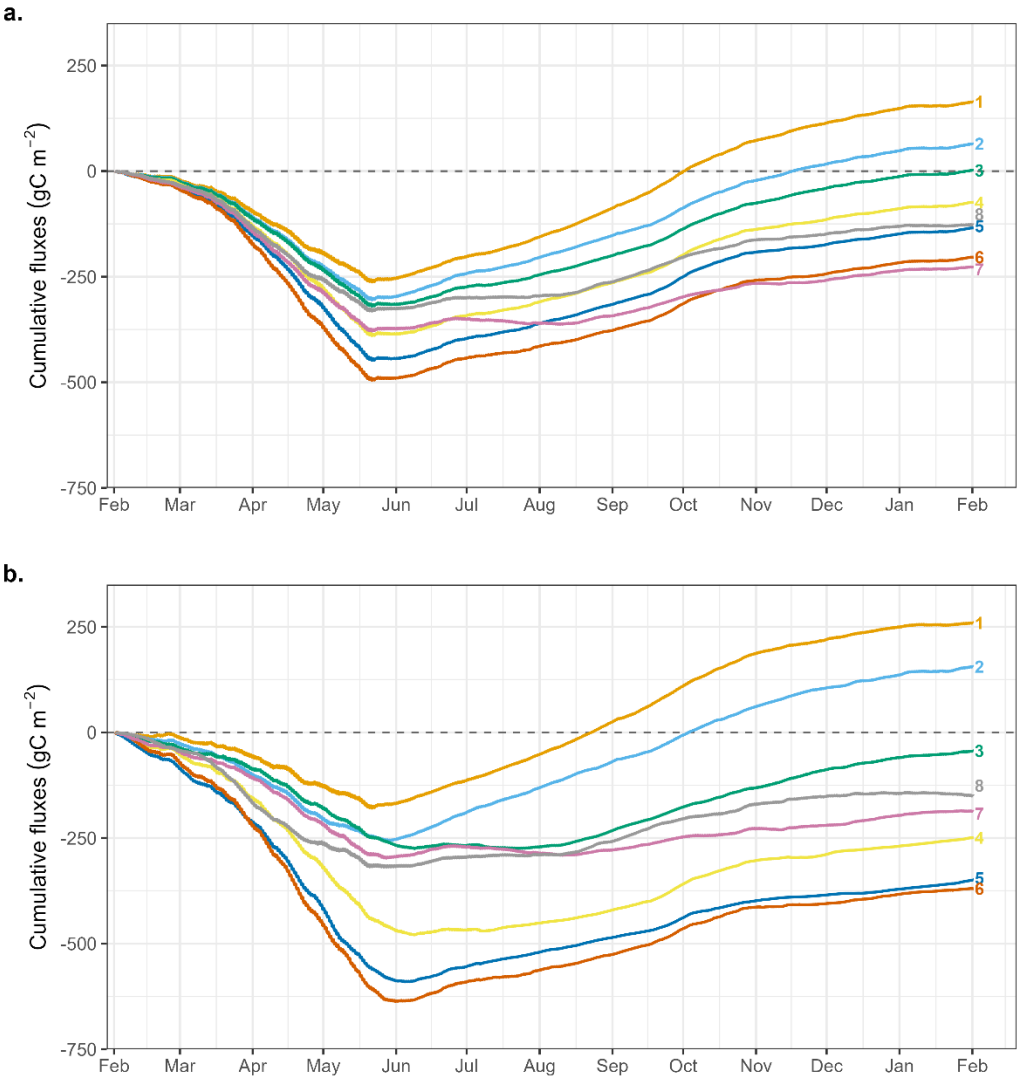
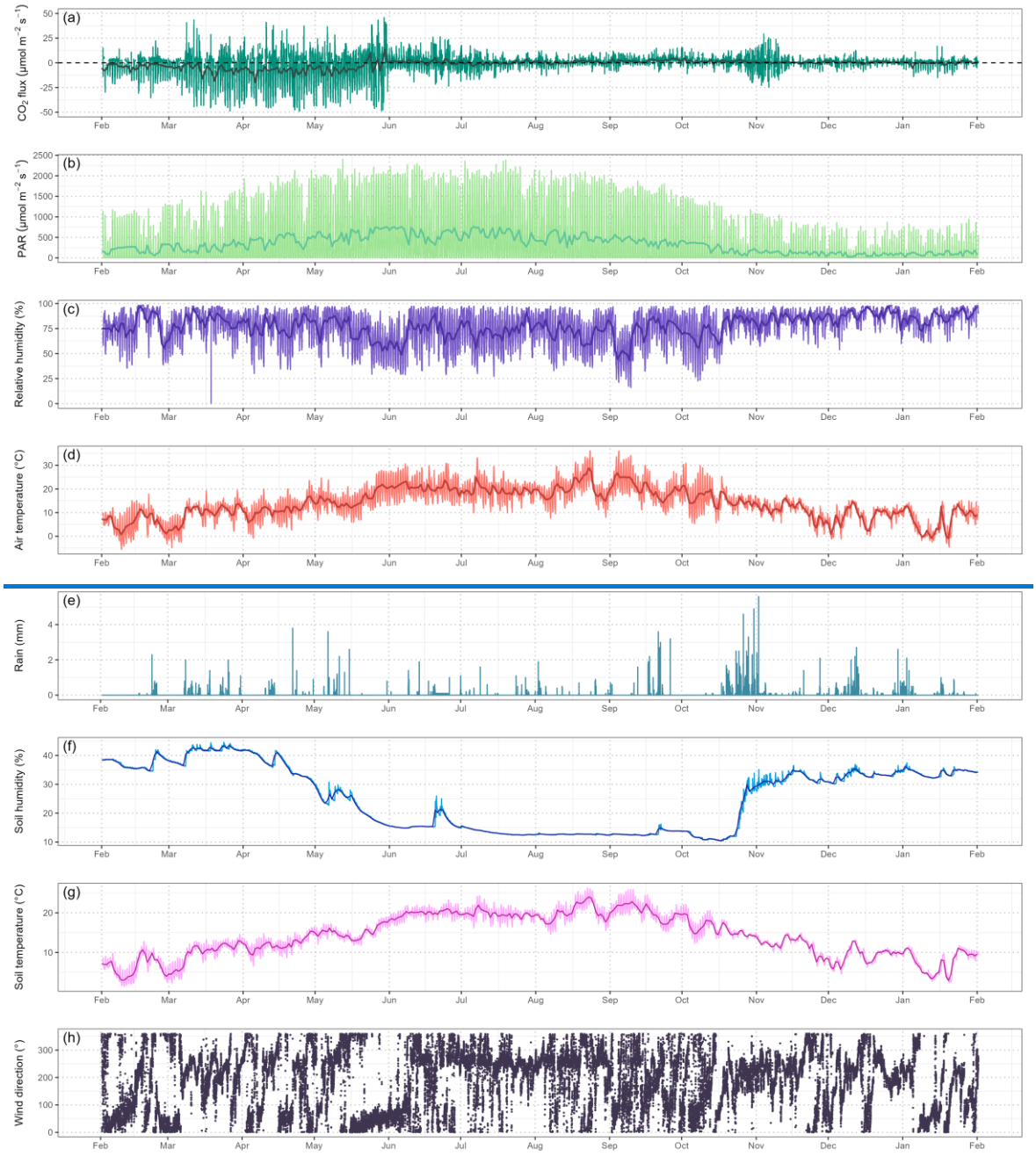
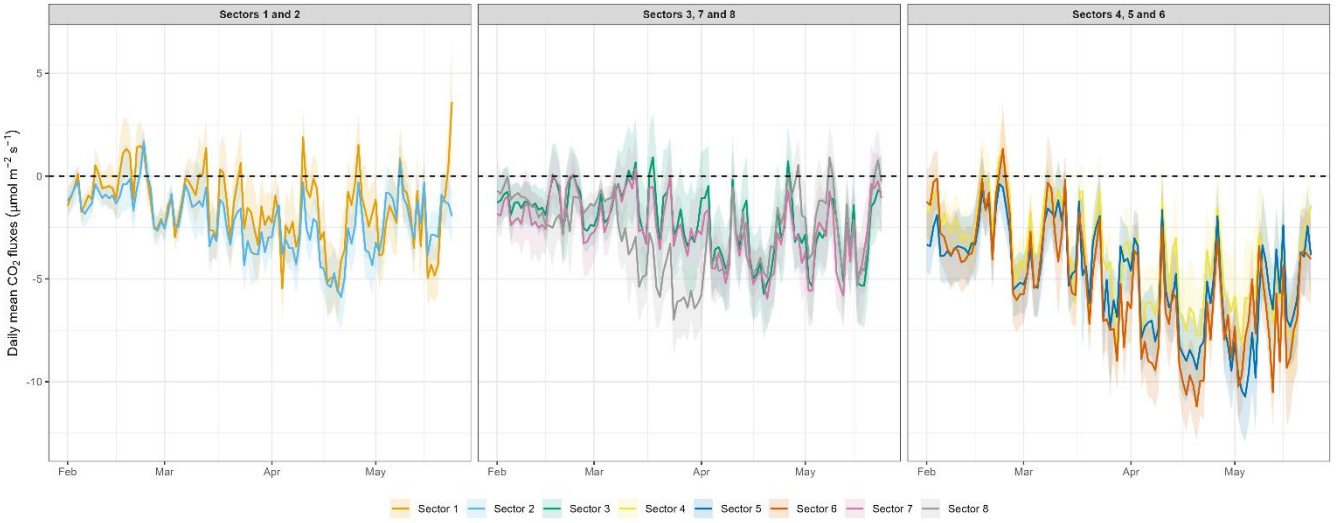


Figure 7~~6~~. Annual cumulative CO_2 ~~(NEE)~~ fluxes (cumulative NEE) reconstructed for each of the eight sectors (Fig. 2a) with~~under~~ the global strategy (a, Scenario 1) and the sector-specific strategy (b., Scenario 2).



3.3 Uncertainties associated with ~~the~~ sector-specific models and ~~the~~ flux footprint

Uncertainty in the sector-specific reconstructions, quantified through the bootstrap 95% confidence interval (IC95) built from B = 100 resampled RF models (Sect. 2.3.4), varied significantly among sectors and between the pre- and post-harvest periods (Tables 1, 2, Fig. 8). Confidence intervals were systematically wider before harvest/mowing (IC95 = 2.41–4.12 µmol m^{-2} s^{-1}) than after (IC95 = 1.28–1.63 µmol m^{-2} s^{-1}), reflecting both the higher intrinsic flux variability during the active growth period and, for several sectors, smaller pre-harvest sample sizes (i.e., n = 625 for Sector 4-before vs. n = 1914 for Sector 4-after). Among the post-harvest/stable periods, the narrowest intervals were obtained for the wheat sub-sectors 4 and 6 (IC95 = 1.28–1.30 µmol m^{-2} s^{-1}), and the widest for Sector 3 (IC95 = 2.39 µmol m^{-2} s^{-1}) and Sector 7 (IC95 = 1.90 µmol m^{-2} s^{-1}).



~~**Figure 8a. Reconstructed CO_2 flux dynamics and bootstrap 95% confidence intervals for each sector, before harvest/mowing (1 Feb.–24 May).**~~

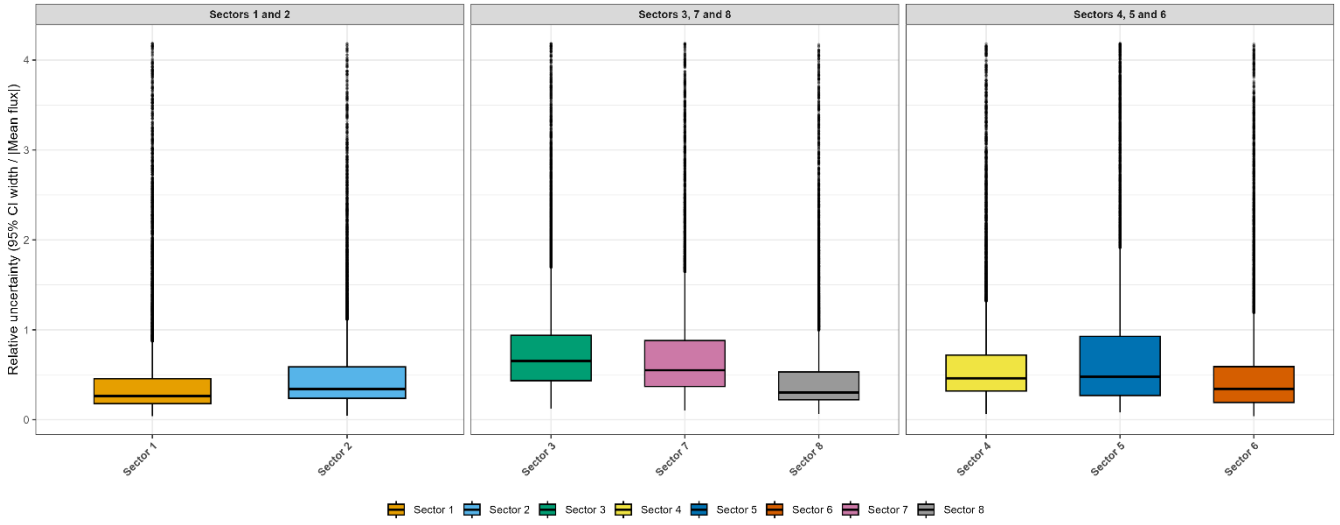


Figure 8. ~~b.~~ Reconstructed NEE dynamics and bootstrap 95% confidence intervals for each sector, before harvest/mowing (1 Feb.–24 May) (above) and ~~As Fig. 8a,~~ distribution of boostrap 95% confidence interval width before harvest/mowing (below).

This pattern reflects both statistical sampling effects and the spatial structure of the flux footprint relative to the position of the EC tower; the implications of this footprint geometry for the interpretation of each sector's cumulative NEE are examined in detail in the Discussion (Sect. 4.2).

3.4 NEE Partitioning ~~of NEE~~ into GPP and ecosystem respiration (R_{eco})

Partitioning of the sector-specific RF-reconstructed NEE into GPP and Reco, following Kowalski et al. (2003, 2004) (Sect. 2.4), was performed for each of the eight sectors and for the combined wheat sector (Sectors 4+5+6) (Table 3, Fig. 9). Across all sectors, annual GPP ranged from −1037 gC m^{-2} (Sector 5) to −1601 gC m^{-2} (Sector 8, grassland), and annual Reco from 684 gC m^{-2} (Sector 5) to 1700 gC m^{-2} (Sector 1) (Table 3).

The three wheat sub-sectors (4, 5, 6) shared a broadly similar phenological signature, i.e. moderate GPP (−1037 to −1419 gC m^{-2}) combined with the lowest Reco values of the whole dataset (684 to 1050 gC m^{-2}), consistent with a single, well-defined crop cycle sampled without interference from adjacent land covers. When combined, Sectors 4+5+6 (i.e. the full wheat field, 133–283°) yielded an annual NEE of −308 gC m^{-2}, GPP of −1298 gC m^{-2} and Reco of 990 gC m^{-2} (Table 3); these combined values fall, as expected, within the range spanned by the three individual sub-sectors, and are closest to Sector 6 (the widest and best-sampled sub-sector, contributing the largest share of observations to the combined estimate; Table 1), while Sector 5 (the sub-sector centred on the sonic-anemometer wake) showed the most negative NEE and the lowest Reco of the three, and Sector 4 the least negative NEE. This internal consistency between the combined estimate and its three constituent sub-sectors supports the reliability of the wheat-field carbon budget as a whole (see also Sect. 3.3, 4.2).

By contrast, Sectors 1 (hybrid transition zone), 2 (mixed grain) and 8 (grassland), despite all lying within angular ranges vegetated for most of the year, displayed markedly different GPP/Reco balances. Sector 8 (grassland) combined the strongest

gross uptake of all sectors (GPP = −1601 gC m⁻²) with a comparatively moderate Reco (1456 gC m⁻²), resulting in the second most negative cumulative annual NEE of the whole site (−145 gC m⁻²) after the wheat sectors. Sector 2 (mixed grain) showed a markedly lower GPP (−1141 gC m⁻²) combined with a high Reco (1292 gC m⁻²), reflecting the loss of photosynthetic activity after the early harvest (24 May) and the subsequent bare-soil respiration; overall, Sector 2 remained a modest net source (+151 gC m⁻²). Sector 1 (hybrid) showed both a high gross uptake (GPP = −1505 gC m⁻², closer to that of the grassland than of the mixed-grain sector) and, simultaneously, the highest Reco of all eight sectors (1700 gC m⁻²), so that despite a photosynthetic capacity comparable to Sector 8, its respiratory term outweighed it and Sector 1 remained the largest net source of the whole site (+195 gC m⁻²). This contrast between Sectors 1, 2 and 8, three sectors adjoining the grassland/mixed-grain area yet showing distinctly different NEE, GPP and Reco combinations , illustrates that superficially similar land-cover labels do not guarantee similar carbon dynamics once the underlying GPP/Reco decomposition is examined (see Sect. 4.3).

Sectors 3 and 7, both defined to isolate the two ditch/riparian corridors (Sect. 2.3.1), occupied an intermediate position relative to the other sectors: their GPP (−1147 and −1295 gC m⁻², respectively) and Reco (1115 and 1114 gC m⁻²) were both closer to the mixed-grain and hybrid values than to the wheat or grassland ones, and both sectors were net, moderate sinks (−32 and −181 gC m⁻², respectively). Given their position immediately adjacent to Sectors 2/1 and 8 (Sect. 3.3), this intermediate GPP/Reco signature is consistent with a footprint integrating both riparian vegetation and edge contributions from the neighbouring crop and grassland fields (see Sect. 4.3).

Table 3. ~~Final~~Annual cumulative estimates of NEE, GPP and Reco (gC m⁻² yr⁻¹) obtained from the Kowalski et al. (2003, 2004) partitioning, for each sector and for the combined wheat sector (Sectors 4+5+6).

	Sector 1	Sector 2	Sector 3	Sector 7	Sector 8	Sector 4	Sector 5	Sector 6	Sector 4+5+6
NEE	195	151	-32	-181	-145	-256	-353	-366	-308
GPP	-1505	-1141	-1147	-1295	-1601	-1056	-1037	-1419	-1298
Reco	1700	1292	1115	1114	1456	800	684	1050	990

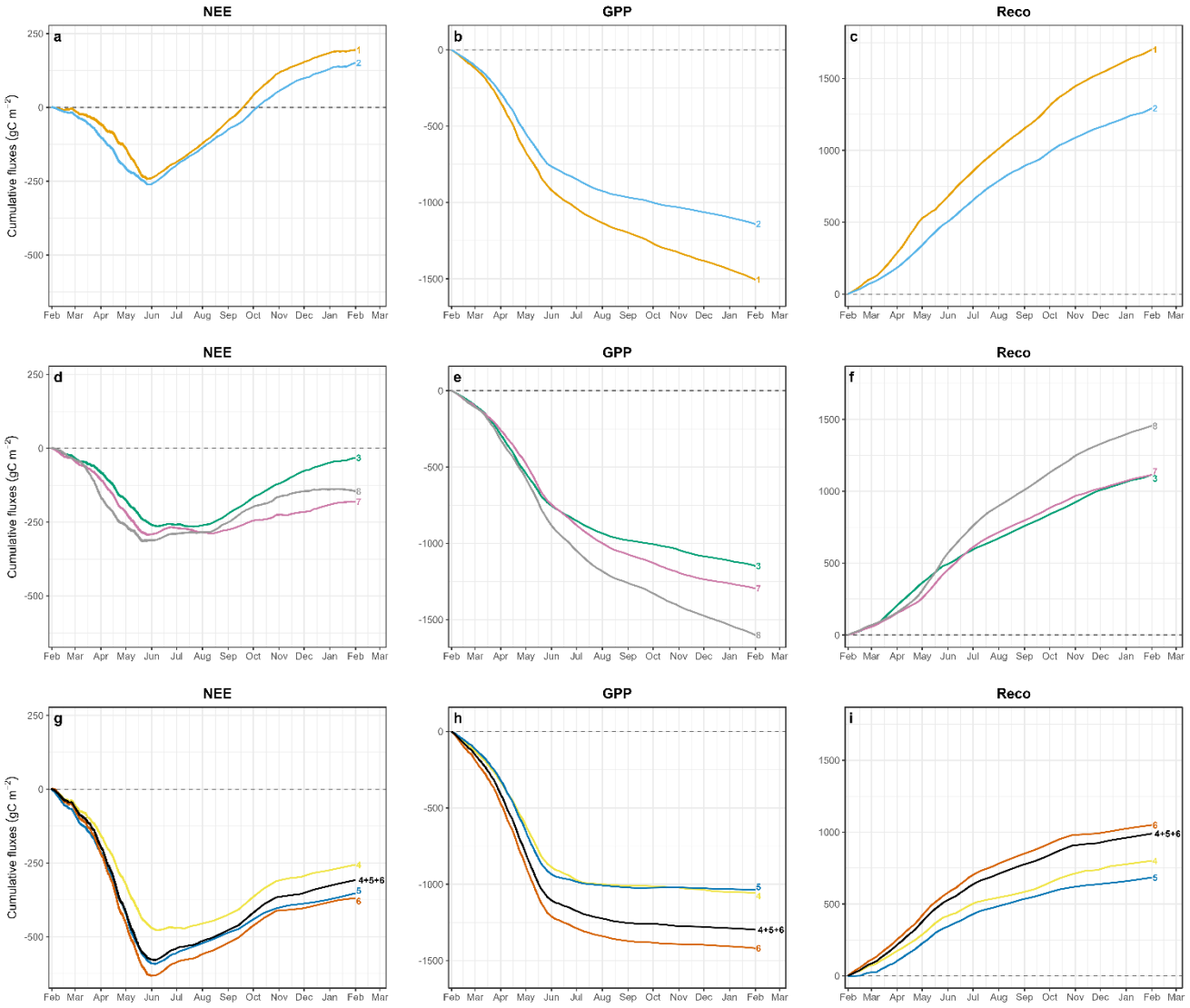


Figure 9. Cumulativeive estimates of NEE, GPP and Reco for each of the eight sectors, obtained from the Kowalski et al. (2003, 2004) partitioning of the sector-specific Random Forest flux reconstructions.

The consistency between this GPP/Reco-based partitioning and the direct RF-based cumulative NEE reconstructed in Sect. 3.2 is examined in the Discussion (Sect. 4.3), together with the implications of the sector-specific phenological and management-driven contrasts identified above.

4 Discussion

4.1 Why sector-specific modelling is required for~~at~~ a heterogeneous single-EC tower site set-up?

The near-equivalence~~,~~ and occasional slight advantage~~,~~ of the global RF model in the OOB point-prediction exercise (Sect. 3.2, Table 2) is best understood as a manifestation of the classical bias-variance trade-off inherent to ensemble tree methods (Breiman, 2001). In OOB validation, both strategies are evaluated only on wind directions that were actually sampled within each sector, i.e. an interpolation exercise within a domain of environmental conditions already encountered during training. In this regime, the global model benefits from a much larger effective training sample ($n \approx 34{,}800$ vs. 600–8,000 for individual sector-specific models), which mechanically narrows its bootstrap confidence intervals (Table 2) and allows the smallest, least-sampled sectors to "borrow" information from the wider dataset, a form of implicit partial pooling. Because wind direction remains an explanatory variable in the global model, the ensemble is, in principle, able to recover part of the sectoral structure from this proxy variable alone; but with mtry = $\lfloor\sqrt{8}\rfloor = 2$, wind direction competes with seven other predictors for selection at each split and is therefore only partially and diffusely "learned" by the global ensemble.

However, this apparent equivalence broke down once fluxes were extrapolated over the full annual cycle for each sector (Sect. 3.2, Fig. 6) — an exercise that, by construction, requires the model to predict flux behaviour for combinations of PAR, air temperature, day-of-year and soil conditions for which each specific sector is often poorly represented in the training data (i.e. a genuine extrapolation regime rather than interpolation). In this regime, the advantage of pooling reverses: when a particular combination of environmental drivers is rare for a given target sector but frequent for the dominant sector in the pooled dataset (Sector 6/wheat, representing the largest single share of the dataset), the corresponding leaves of the global RF trees become populated mainly by the dominant sector, so that the global model's prediction for the target sector regresses toward the pooled, dominant-sector response — a shrinkage effect conceptually related to partial pooling in hierarchical models and, in its net numerical consequence, to Simpson's-paradox-type aggregation bias. This mechanism is consistent with the observation that the least-sampled sectors (2, 4, 5) showed the strongest compression of their annual NEE values under the global strategy (−59 to −70%; Sect. 3.2), while the best-sampled sector (Sector 6) showed the smallest compression (−45%). Sector 3, whose sector-specific NEE was already close to zero (−44 gC m^{-2}), showed an even more extreme manifestation of this shrinkage, with its cumulative NEE collapsing to near zero (+2 gC m^{-2}) under the global strategy rather than being merely compressed in magnitude. The exceptional amplification observed for Sector 7 indicates that this shrinkage is not a simple function of sample size alone, but also depends on the proximity, in covariate space, between the target sector and the dominant sectors that "contaminate" its predictions — a proximity that can act in either direction depending on the local structure of the fitted trees. Ecologically, this divergence is consistent with the fact that day-of-year is only an imperfect proxy for phenological stage: at a given day-of-year, the wheat, mixed-grain and grassland covers can be at very different ~~developmental~~phenological stages, and a global model that only weakly resolves sector identity through wind direction will tend to average out these physiologically distinct crop responses. This supports the conclusion, drawn in Sect. 3.2, that a single pooled RF model is not adequate for reconstructing field-scale annual ~~carbon budgets~~cumulative NEE values at a sub-field-heterogeneous site such as

ours, even though it may appear competitive - or even preferable in terms of confidence-interval width - in a standard point-validation exercise as done in the present study. This distinction between the two validation regimes (interpolation vs. extrapolation) has a broader methodological implication for flux-partitioning studies relying on machine-learning gap-filling at heterogeneous sites: OOB or cross-validation metrics computed only on already-sampled conditions may substantially under-estimate the practical cost, in terms of annual NEE ~~budget~~ bias, of pooling data across ecologically distinct source areas. This finding also reinforces the argument, raised in the Introduction, that resolving spatial heterogeneity within EC footprints - whether through footprint modelling and land-cover attribution (Chen et al., 2011), multi-tower designs (Oren et al., 2006), or alternative statistical approaches (Wang et al., 2016) - remains a prerequisite for deriving physically meaningful, field-scale ~~carbon budgets~~annual NEE from single-tower EC records over heterogeneous agricultural mosaics. In this respect, the wind-sector RF approach used here, combined with the increasing availability of low-cost EC hardware (Cunliffe et al., 2022; van Ramshorst et al., 2024; Callejas-Rodelas et al., 2025; Rannik et al., 2026), offers a practical, scalable pathway to improve the spatial representativeness of single-tower flux monitoring in mosaic landscapes, without the cost and logistical burden of a full multi-tower network. For this reason, and consistent with Sect. 3.2, the remainder of this Discussion (Sects. 4.2–4.3) focuses exclusively on the sector-specific (Scenario 2) reconstructions.

4.2 Model and experimental uncertainties: the role of the flux footprint and tower position

Beyond the purely statistical uncertainty captured by the bootstrap confidence intervals (Sect. 3.3, Table 2, Fig. 8), the reliability of the sector-specific ~~carbon budgets~~NEE values derived in this study is fundamentally constrained by the spatial structure of the EC flux footprint and by the fixed position of the tower relative to the surrounding land-cover mosaic (Fig. 2a). Because a single EC system was used, the "sector" attribution of each 10-min flux value is only as reliable as the assumption that the footprint for that wind direction is dominated by the target land cover; this assumption holds to very different degrees across the eight sectors defined in this study.

For the wheat field, sampled through the wide~~,~~ uninterrupted angular range of Sectors 4, 5 and 6 (133–283°), this assumption is comparatively well supported: no ditch, canal or riparian corridor lies within this angular range, and the footprint can reasonably be considered to sample the wheat canopy (and, secondarily, bare or senescent soil after harvest) almost exclusively. Confidence intervals for these three sub-sectors, particularly after harvest (IC95 = 1.28–1.30 µmol m^{-2} s^{-1}; Table 2), are also among the narrowest of the whole dataset. Together, these two independent lines of evidence - a spatially "clean" footprint and comparatively narrow statistical uncertainty - support together the interpretation that the reconstructed NEE, GPP and R_{eco} values for the wheat field (Sects. 3.2–3.4; Table 3) represent a genuinely well-constrained cumulative annual NEE ~~carbon budget~~ value~~(BC)~~ for this parcel, one of the more robust outcomes of the present~~is~~ study.

The situation is markedly less favourable for Sectors 1, 2, 3 and 7. Sectors 3 and 7 were explicitly defined to isolate the two ditch corridors and their riparian margins (Sect. 2.3.3); even so, given the narrow width of these features relative to the extent of the EC footprint (Kljun et al., 2015; Kumari et al., 2020), some contribution from the flanking crop or grassland edges cannot be excluded, and, conversely, some contribution from the ditch/riparian vegetation is very likely to persist within the

crop-labelled sectors immediately adjacent to it (Sectors 1 and 2). This is consistent with the comparatively wide confidence intervals obtained for Sectors 3 and 7 (IC95 = 2.39 and 1.90 µmol m^{-2} s^{-1}, respectively; Table 2) and with the largest discrepancy found between the RF-based and Kowalski-partitioned cumulative NEE value~~,~~ for Sector 1 ($\Delta \approx 64$ gC m^{-2}, ≈ 25%; Sect. 3.4). We therefore consider that, for the mixed-grain (Sector 2) and hybrid transition zone (Sector 1) in particular, the reconstructed yearly cumulative ~~carbon budgets~~NEE values cannot be interpreted as unambiguous~~,~~ parcel-specific values in the same way as for the wheat sectors: they are best regarded as composite ~~budgets~~NEE values integrating a variable, and currently unquantified, contribution from riparian vegetation and open-ditch surfaces.

The permanent grassland (Sector 8) occupies an intermediate position. Visually and statistically, its footprint appears comparatively little affected by the adjacent ditch network, and its confidence interval (IC95 = 1.80 µmol m^{-2} s^{-1}) is only slightly wider than that of the wheat sectors, while the discrepancy between its RF-based and partitioned NEE estimates was the smallest of all eight sectors ($\Delta \approx 1$ gC m^{-2}; Sect. 3.4). While this sector's cumulative NEE value~~budget~~ cannot be considered as unambiguously "pure" as that of the wheat field, given its position adjacent to the drainage-ditch network, the convergence of these independent lines of evidence suggests that it is comparatively reliable, and markedly less exposed to footprint contamination than the mixed-grain, hybrid or ditch sectors.

Overall, these results indicate that the practical outcome of a single-tower, wind-sector RF approach in a heterogeneous agricultural landscape does~~is~~ not give a uniformly precise ~~carbon budget~~annual cumulative NEE value for every land cover, but rather a gradient of confidence directly related to the local footprint geometry: high confidence for spatially "isolated" covers such as the wheat field (and, to a slightly lesser extent, the grassland), and comparatively lower confidence for covers immediately adjacent to linear landscape features such as drainage ditches. Explicit footprint modelling with land-cover attribution (e.g. Kljun et al., 2015; Chen et al., 2011), applied at finer temporal resolution than the sector-averaged approach used here, or complementary plot-scale chamber measurements deployed within specific sectors, would be valuable next steps to further quantify, and potentially correct for, this residual footprint-mixing uncertainty in the mixed-grain, hybrid and ditch sectors.

4.3 Consistency between direct NEE reconstruction and GPP/R_{eco} partitioning

Comparing the yearly cumulative NEE deduced from the GPP/Reco partitioning (Table 3, Sect. 3.4) with the direct RF-based cumulative NEE obtained under the sector-specific strategy (Sect. 3.2, Fig. 7) shows overall good agreement, with sector-dependent discrepancies. For most sectors, the two estimates differ by less than 15 gC m^{-2} (< 10%): Sector 3 (−30 vs. −32 gC m^{-2}), Sector 4 (−244 vs. −256 gC m^{-2}), Sector 5 (−348 vs. −353 gC m^{-2}), Sector 6 (−370 vs. −366 gC m^{-2}), Sector 7 (−187 vs. −181 gC m^{-2}) and Sector 8 (−146 vs. −145 gC m^{-2}), and the combined wheat sector shows essentially identical values (−308 gC m^{-2} under both approaches). Larger, though still moderate, discrepancies are found for Sector 1 (+259 vs. +195 gC m^{-2}, a difference of 64 gC m^{-2}, ≈ 25%) and, to a lesser extent, Sector 2 (+136 vs. +151 gC m^{-2}, a difference of 15 gC m^{-2}, ≈ 11%). These two sectors are precisely those identified in Sect. 3.3 and 4.2 as most exposed to footprint mixing with riparian vegetation and ditch surfaces, suggesting that the Kowalski partitioning, which separates fluxes on the basis of a day/night, PAR-driven

criterion rather than by land-cover contribution, may be differentially sensitive to the additional respiratory or photosynthetic signal contributed by non-target surfaces within the footprint. This overall convergence between two independent methods (direct RF reconstruction vs. light-response partitioning) provides confidence that the underlying GPP/Reco decomposition (Table 3, Fig. 9) is a robust basis for comparing the carbon-flux dynamics of the different sectors.

Beyond this consistency check, the GPP/Reco decomposition offers a more mechanistic view of why sectors bearing superficially similar land-cover labels can nonetheless display markedly different net carbon budgets (Sect. 3.4). The three wheat sub-sectors (4, 5, 6) shared a common phenological trajectory dominated by a single, well-defined annual crop cycle, so that their individual GPP and Reco values, and those of the combined Sectors 4+5+6, remained close to one another and reflected essentially the same underlying process: a strong, synchronous photosynthetic pulse during spring growth followed by a sharp decline in both GPP and Reco after harvest (7 July). This internal consistency across spatial subdivisions of a single, homogeneous field supports treating Sectors 4+5+6 as a genuine field-scale carbon budget for winter wheat.

By contrast, Sectors 1, 2 and 8 illustrate how similar apparent vegetation cover can conceal contrasting carbon dynamics. Sector 8 (grassland) combined the highest GPP of the whole site with a moderate Reco, consistent with a continuously vegetated, perennial cover subject to grazing rather than harvest, which sustains photosynthetic activity later into the season without the abrupt post-harvest respiration pulse seen in annual crops. Sector 2 (mixed grain), despite sharing an annual-crop phenology broadly similar to wheat before its early harvest (24 May), displayed a much lower GPP and a comparatively high Reco, indicating a shorter and less productive growing period combined with sustained soil respiration on bare ground for most of the year. Sector 1 (the hybrid transition zone between grassland and mixed grain, including riparian vegetation) combined a GPP close to that of the grassland (Sector 8) with the highest Reco of the whole site, i.e. it behaves neither as a "pure" grassland nor as a "pure" cropland, but as a composite signal integrating perennial photosynthetic capacity with elevated, likely riparian- and ditch-driven, respiration; this explains why Sector 1, despite substantial gross uptake, is the largest net carbon source identified in this study (Sect. 3.4).

Sectors 3 and 7 (the two ditch/riparian corridors) further illustrate this gradient: their GPP and Reco values lie between those of the crop/grassland sectors and those of Sector 1, and both remain modest net sinks. Given their position directly adjoining Sectors 2 and 8 respectively (Sect. 2.3.1, 3.3), this intermediate signature is consistent with these sectors sampling a mixture of open-ditch/riparian surfaces and edge contributions from the neighbouring vegetated parcels, rather than a fully homogeneous, non-vegetated ditch surface. Taken together, these results show that the wind-sector RF/partitioning approach, beyond providing annual NEE, GPP and Reco values, allows a differentiated reading of within-site phenological and management-driven contrasts that a single pooled model, or a coarser land-cover classification, would not resolve (Sect. 4.1).

4.1 Methodological considerations: single-tower sector partitioning and modelling

Deploying a single Eddy Covariance (EC) tower with wind-sector partitioning enabled the continuous monitoring of multiple adjacent agricultural land covers, representing a cost-effective alternative to multi-tower setups. This approach reduces instrumentation and maintenance costs but inevitably introduces spatial uncertainties in heterogeneous landscapes. The EC flux footprint may encompass several vegetation types depending on wind direction, measurement height, surface roughness, and the stability of atmospheric conditions. Under unstable conditions, the footprint remains narrow and is typically dominated by a single surface type; however, because turbulent exchange is strongest near the tower under such conditions, the relative contribution of nearby elements, such as ditches and riparian vegetation, becomes more pronounced. Conversely, under stable conditions, the footprint expands and integrates fluxes over a larger upwind area, which may include multiple fields and dilute the ditch's influence within the aggregated signal. As demonstrated by Hernandez-Rodriguez et al. (2023), such organized heterogeneity can modify observed fluxes by more than 10% compared with a homogeneous land-cover assumption.

In this study, three monitored sectors (grassland, mixed grain, and hybrid) are directly adjacent to a drainage ditch, whereas the wheat field lies farther away and is unaffected by aquatic surfaces. The ditch and its riparian vegetation contribute additional CO_2 fluxes that cannot be spatially discriminated within the EC footprint. Consequently, fluxes attributed to the grassland, mixed grain, and hybrid sectors may partly integrate emissions or uptake from the ditch, while the wheat sector provides a purely terrestrial reference. The sector-based strategy therefore associates each flux measurement with the predominant upwind vegetation type (e.g., wheat versus grassland), but this attribution remains imperfect due to the variable footprint geometry. Multi-tower configurations would offer more precise parcel-level discrimination but involve substantial financial and logistical constraints. Hence, the single-tower, wind-sector approach adopted here represents a pragmatic compromise: it enables continuous, multi-cover flux monitoring within a mosaic of agricultural fields and wetland interfaces while accepting a controlled level of footprint mixing and the associated uncertainty. This evaluation framework maintained consistency while allowing direct comparison between sector-specific and global modelling strategies.

Given its narrow width of approximately 12 m, the Brune ditch represents only a minute fraction of this footprint and cannot generate a dominant or isolable signal within the turbulent flow. Moreover, the ditch is not aligned with the main axis of the EC tower, making it geometrically impossible to define a wind sector that would exclusively sample fluxes from its surface. Any such sector would inevitably include contributions from adjacent vegetation and soil surfaces, especially from the riparian strip bordering the ditch.

EC measurements complemented by Random Forest (RF) modelling allowed upscaling and gap-filling of flux data across the different systems, incorporating vegetation specific and management information. The RF models were robust across land covers, with high performance. However, while global and crop specific models achieved similar accuracy metrics, their ecological behaviour differed markedly. The global model tended to average flux behaviour across systems, obscuring specific phenological and management driven variability. For example, it failed to capture the specific productivity phases of each crop and showed muted responses to events such as harvest. In contrast, sector specific models revealed meaningful ecological patterns and management effects. These models distinguished between gradual, drought induced NEE declines and the abrupt flux reversals after harvest. They also identified crop specific daytime ($NEE_{daytime}$) and nighttime ($NEE_{nighttime}$) flux partitioning, accurately reflecting physiological processes. Distinct $NEE_{daytime}$ profiles emerged: wheat showed intense spring uptake that ended abruptly at harvest, grassland showed modest but continuous uptake throughout the season, and the mixed-grain and hybrid systems diverged after May's harvest (the mixed-grain parcel became essentially bare, whereas the hybrid parcel, containing riparian vegetation by the ditch, maintained some photosynthetic activity). These differences mirror results from other studies: for example, Bajgain et al. (2018) found that winter wheat had much higher peak daytime uptake than tallgrass prairie, and that the wheat site became a net carbon source annually whereas the prairie remained a sink. Such nuanced dynamics are essential to understand carbon cycling and management impacts across diverse agroecosystems.

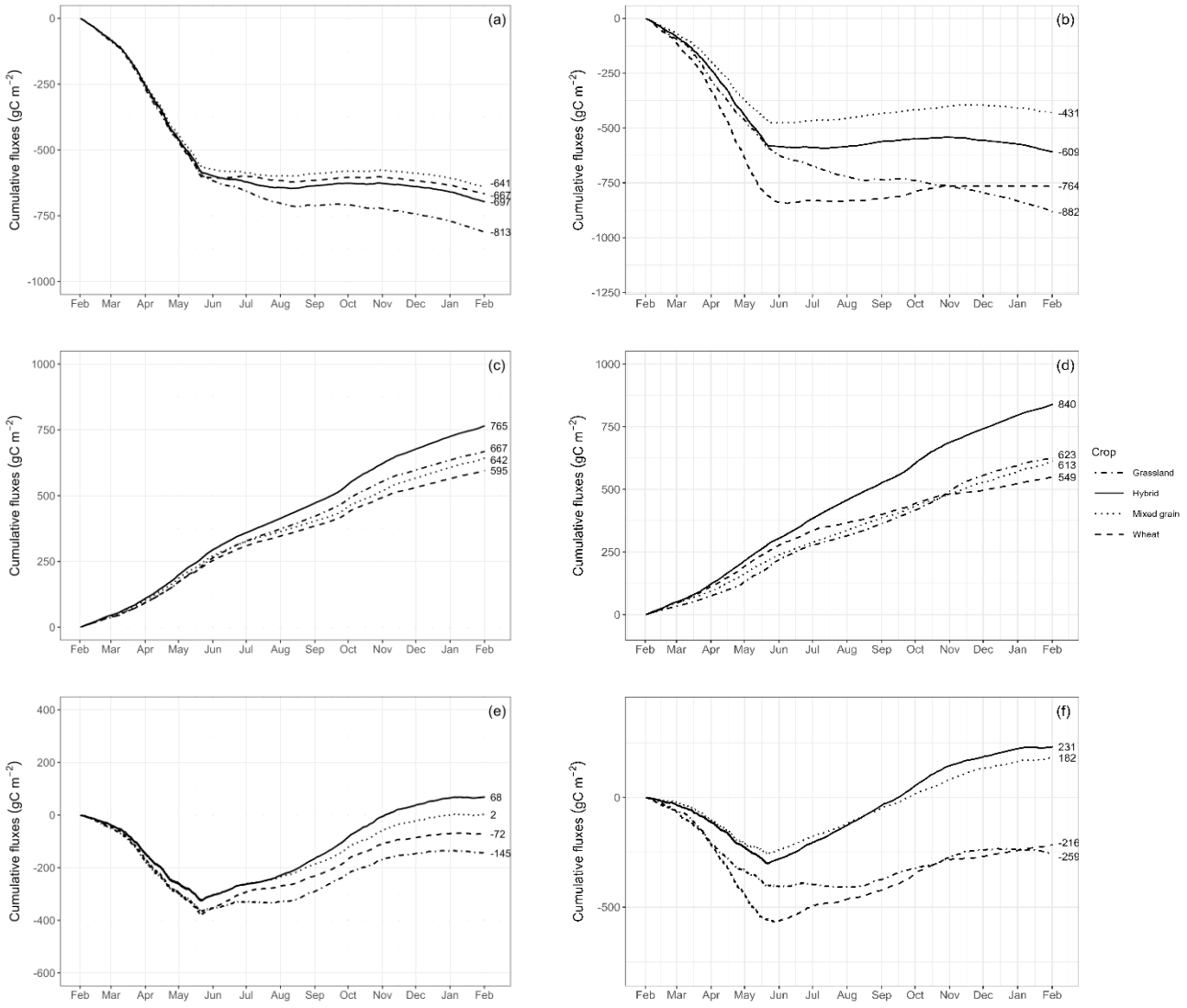


Figure 9. Cumulative CO_2 fluxes by vegetation type and modelling approach, with panels (a), (c), and (e) corresponding to Scenario 1 (global model) and panels (b), (d), and (f) to Scenario 2 (crop-specific models). Panels (a) and (b) represent daytime CO_2 assimilation ($NEE_{daytime}$), panels (c) and (d) nighttime CO_2 emission ($NEE_{nighttime}$), and panels (e) and (f) the net cumulative CO_2 exchange. Each curve reflects a specific land cover. Final cumulative values indicate the carbon balance (gC m^{-2} y^{-1}) and the respective contributions of $NEE_{daytime}$ and $NEE_{nighttime}$ (gC m^{-2}).

Despite the RF models' overall robustness, performance declined for the wheat sector after harvest. This lower performance does not reflect a fundamental modelling issue, but rather the specific conditions under which the EC measurements were collected during that period. During a series of storms in November, intense rainfall, strong atmospheric turbulence, and rapidly shifting wind directions occurred. During these storm events, the prevailing wind directions caused the EC system to

predominantly sample fluxes originating from the wheat sector, even though the disturbance was not specific to that land cover. The combination of precipitation and wind-driven turbulence generated large spikes in the CO_2 signal, leading to spurious flux values that did not represent actual ecosystem exchange. These anomalies were not linked to environmental variability or management practices but instead resulted from temporary disturbances of the measurement system during the storm events. Although part of this noise was removed during preprocessing, some anomalous values could not be fully filtered and therefore remained in the dataset. Consequently, the RF models (both global and sector-specific), which rely on environmental drivers to explain flux variability, were unable to relate these erratic values to any meaningful explanatory variables and failed to reproduce them. In this context, the reduced model performance is not problematic. On the contrary, it indicates that the models do not assimilate or reproduce physically unrealistic fluxes. Importantly, these distorted values were not included in the final predicted time series used for carbon budget calculations. By effectively replacing these anomalies with fluxes consistent with ecologically plausible responses to environmental drivers, the model prevents the propagation of erroneous data and reinforces the reliability of the model-based flux estimates.

To validate the EC-based flux measurements and Random Forest (RF) modelling, static and automated chamber measurements are highly informative. Wang et al. (2013) reported near-identical NEE values using EC and automated chambers in winter wheat, with seasonal EC estimates of −251 gC m^{-2} and chamber-derived values of −205 gC m^{-2}. Similarly, Drewer et al. (2017) found consistent patterns between chamber and EC fluxes in intensively managed grasslands. These studies indicate that chamber measurements can reliably reflect EC fluxes at plot scale and can also capture temporal dynamics (e.g. drought responses or post-harvest changes). Although chamber data have limited spatial coverage, they offer crucial plot-scale insight and could help verify RF model accuracy, especially under flux footprint conditions that are highly localized.In the future, to validate the EC-based flux measurements and Random Forest (RF) modelling approaches at the studied site, static and automated chamber measurements could be deployed simultaneously over each crop at different locations inside the footprint and key time (seasonal, diurnal) periods linked to phenology and management. Indeed, some studies indicate that chamber measurements can reliably reflect EC fluxes at plot scale and can also capture temporal dynamics (e.g. drought responses or post-harvest changes). For instance, Wang et al. (2013) reported near-identical NEE values using EC and automated chambers in winter wheat, with seasonal EC estimates of −251 gC m^{-2} and chamber-derived values of −205 gC m^{-2}. Similarly, Drewer et al. (2017) found consistent patterns between chamber and EC fluxes in intensively managed grasslands. Although chamber data have limited spatial coverage, along EC measurements, both techniques run simultaneously can offer crucial plot-scale insight and could help verify RF model accuracy, especially under flux footprint conditions that are highly localized.

Given the consistently superior performance and ecological coherence of the sector-specific models, all subsequent discussion will focus exclusively on their results.

We thank the reviewer for this valuable comment. We agree that the limitations of the study should be more explicitly discussed. In the revised manuscript, we will expand the Discussion section to better acknowledge the uneven distribution of observations among vegetation types and the implications of using NEE without flux partitioning.

EC measurements have limitations, including energy budget closure, equipment costs, and technical challenges in data processing. But I am inclined to argue that short gaps during maintenance and rainfall are the limitations, as these gaps are trivial. The assumption of EC measurements is homogeneous field across the fetch; thus EC is not applicable to sites with high footprint heterogeneity. This is not a limitation of EC measurement itself; the challenge is separating the footprints for this complicated mosaic.

-

We thank Professor Sun for his feedback and agree with him about EC measurement limitations/challenges due to i) sensor maintenance/issue period without any measured fluxes that need to be gapfilled and ii) heterogenous site with different habitats seen differently in time and space according to wind directions/speeds. It is particularly true after having deployed several EC towers these last years since years of 2010's either over homogenous (less heterogenous) tidal flats, salt marsh systems (Polsenaere et al., 2012, bg-9-249-2012 and Mayen et al., 2024, bg-21-993-2024) or hereafter over clearly heterogenous sites with different habitats around the EC mast as carried out in the present study for instance. This is the reason why, owing to RF modeling tool improvements, we propose our combined measured and modelled EC flux approach that, we believe, can overcome these limitations and proved EC measurements can be done over such heterogenous crop field to have at the end consistent estimated flux (NEE) values for each parcel seen by EC sensors. In this way and as risen by all Referees, we significantly modified the manuscript in turn with further computations especially for better constrain and quantify NEE values coming from each parcel.

We also note that the interpretation of Eddy Covariance measurements in heterogeneous environments is fundamentally linked to the spatial structure of the flux footprint. In our study, this aspect is explicitly addressed through the sector-based framework introduced in Fig. 2a (submitted MS), which provides a directional decomposition of the contributing source areas. This representation is essential for our analysis, as it allows us to directly relate the reconstructed fluxes to the surrounding land-use mosaic. This is particularly important for sector 2 (70°–103°), where multiple land cover types are simultaneously present within the footprint, including grassland, mixed grain fields, and riparian vegetation along the Brune canal. As already outlined in the introduction section of the submitted MS, this configuration does not correspond to a single dominant source area, which complicates the attribution of the observed CO_2 signal and justifies a sector specific treatment. By contrast, the wheat-dominated sector (133°–283°) presents a much more homogeneous footprint, with a single crop type largely controlling the measured fluxes. In this case, the sectorisation confirms that the Eddy Covariance assumptions are much more closely met,

and the interpretation of the reconstructed fluxes is correspondingly more direct. Nevertheless, even in this more homogeneous configuration, additional sources of uncertainty remain, as discussed in detail in response to Reviewer 2.

4.2 Seasonal NEE dynamics: phenological, environmental controls and management

Seasonal patterns of $NEE_{daytime}$ and $NEE_{nighttime}$ varied markedly between land covers and were primarily shaped by phenology, management practices, and environmental constraints. In spring, wheat exhibited the highest rates of daytime CO_2 uptake, with peak productivity in mid-May. This strong early-season sink surpassed that of the grassland, which maintained a more stable but lower carbon uptake throughout the season. These patterns are consistent with findings by Gilmanov et al. (2003), who reported higher gross primary productivity (GPP) in winter cereals compared to temperate grasslands during early phenological stages, due to faster canopy development and higher photosynthetic capacity before senescence or management interventions. For reference, the ditch runs along the mixed-grain, hybrid, and grassland parcels but does not border the wheat parcel, which may partly explain the observed differences.

In contrast, the mixed-grain and hybrid sectors initially displayed nearly identical $NEE_{daytime}$ patterns. Prior to the May 24th harvest, both sectors showed similar CO_2 uptake levels, indicating that the hybrid fluxes were dominated by the adjacent mixed-grain plot. After the harvest, however, their dynamics diverged. The mixed-grain sector became essentially bare soil and its daytime sink collapsed, whereas the hybrid sector maintained some photosynthetic activity thanks to the ditch and its riparian vegetation (a strip of grasses and shrubs). This riparian vegetation likely explains why the hybrid sector showed consistently higher $NEE_{nighttime}$ emissions than the pure grassland or mixed-grain sectors, since moist riparian zones are known to sustain elevated respiration due to their higher soil moisture and organic content (Reichstein et al., 2005).

Wheat, on the other hand, transitioned from a carbon sink to a source between mid-May and mid-June as rapid senescence set in. This senescence was likely accelerated by rising temperatures and the onset of drought, making it difficult to distinguish natural maturation from stress responses. At the same time, the grassland experienced gradual reductions in $NEE_{daytime}$, but it never fully ceased assimilation. As a perennial system with only partial grazing (biomass removal by cattle rather than complete mowing), the grassland continued to photosynthesize at a low level even during the driest period. In short, agricultural management drove different flux shifts: the cereal harvest in the mixed-grain parcel caused an abrupt flux reversal, whereas grazing in the grassland produced more moderate, progressive changes. These observations align with Heimsch et al. (2021) and others, who have reported sharper CO_2 flux reversals following harvest compared to grazing in temperate agricultural systems.

The mid-May drought had distinct, asynchronous effects across the systems. In wheat, any drought impact on $NEE_{daytime}$ was largely masked by the overlapping senescence. In the mixed-grain sector, the drought coincided with the interval immediately

~~before harvest; any reduction in uptake was ultimately hard to separate from the imminent harvest removal. By contrast, the grassland showed a clear and sustained reduction in $NEE_{daytime}$ during and after the dry spell, likely due to stomatal closure in response to elevated vapor pressure deficit (VPD). This is consistent with results reported by Flanagan and Adkinson (2011) for temperate grasslands, where water-limiting conditions led to significantly reduced CO_2 uptake.~~

~~Across all land covers, the primary environmental drivers of $NEE_{daytime}$ were light (photosynthetically active radiation, PAR), air temperature (T_a) and VPD. Peak CO_2 uptake occurred on sunny, mild days: for example, maximum assimilation occurred at PAR ≈ 1700 µmol m^{-2} s^{-1}, T_a ≈ 22°C and VPD ≈ 1.2–1.3 kPa (values similar to optimal conditions reported for winter wheat by Wagle et al. (2018). Conversely, hot and dry conditions (high VPD) strongly suppressed photosynthesis and enhanced respiration. Nighttime fluxes remained relatively stable, but $NEE_{nighttime}$ rose modestly with higher temperature and following disturbance events, especially in the hybrid and grassland sectors where plant residues and living vegetation persisted. In particular, the hybrid sector's riparian vegetation and the grassland's residual biomass fuelled elevated microbial and plant respiration at night. These temporal dynamics underscore the tight coupling between phenological development, disturbance regimes and microclimatic conditions in shaping seasonal carbon fluxes in these agroecosystems.~~

~~In parallel, an alternative approach (Scenario 2) separate RF models were trained for each landscape-based wind sector classification area and key temporal subdivision, accounting for phenological shifts such as crop harvest for instance that influence flux dynamics over the wheat and mixed-grained areas. Specifically, for each crop parcel, pre- and post-harvest periods were modelled independently to better capture ecosystem transitions, resulting in seven sector-specific models overall (Table 1). Both strategies used the same explanatory variables described in Section 2.3.3 to ensure comparability and comparison.~~

~~4.3~~4.4 Annual NEE estimates ~~Carbon Budgets~~ of the studied parcels and implications for carbon accounting and limitations

Annual cumulative NEE, GPP and Reco values derived from the Kowalski et al. (2003, 2004) partitioning (Table 3, Sect. 3.4) provide the reference carbon-flux estimates discussed here, given their close agreement with the direct RF-based reconstructions for every sector (Sect. 4.3). Considered together, these values reveal contrasting carbon budgets among the four land covers of the site: the permanent grassland (Sector 8) and the winter wheat field (Sectors 4+5+6) acted as net carbon sinks (−145 and −308 gC m^{-2} yr^{-1}, respectively), whereas the mixed-grain field (Sector 2) and the hybrid transition zone (Sector 1) behaved as net carbon sources (+151 and +195 gC m^{-2} yr^{-1}). However, the confidence that can be placed in each of these values differs markedly according to the footprint considerations discussed in Sect. 3.3 and 4.2.

The winter wheat carbon budget can be considered the most robust of the site (Sect. 3.3, 4.2). The combined estimate for Sectors 4+5+6 (NEE = −308 gC m^{-2} yr^{-1}) is well bracketed by its three constituent sub-sectors (NEE from −244 to −370 gC

m^{-2}; Sect. 3.4), whose differences mainly reflect the angular width, and therefore the sampling density, each sub-sector received (Table 1) rather than genuine differences in the underlying crop: Sector 6, the widest and best-sampled sub-sector, dominates the combined estimate, while Sector 5 (centred on the sonic-anemometer wake, and thus more strongly affected by the u* filtering constraints described in Sect. 2.3.1) shows the most negative NEE of the three. This internal agreement between the combined wheat estimate and its sub-sectors, together with a footprint essentially free of ditch or riparian contamination (Sect. 3.3), supports a genuinely field-scale wheat carbon budget. This sink strength is broadly consistent with other reported values for winter wheat (Table 4); for instance, Schmidt et al. (2012) found ≈ -270 gC m^{-2} yr^{-1} over two years of EC measurements, and Wang et al. (2013) reported -251 gC m^{-2} for a growing season using EC, in close agreement (within 7%) with automatic-chamber estimates.

The permanent grassland (Sector 8) carbon budget can be considered more or less robust: its footprint (Sect. 3.3) is comparatively little exposed to the drainage-ditch network relative to Sectors 1, 2, 3 and 7, since only the margin of the secondary ditch lies within its angular range, so that the reconstructed budget predominantly reflects genuine grassland photosynthesis and respiration rather than a substantial mixed riparian or aquatic contribution. Its confidence interval (Table 2) is only slightly wider than that of the wheat sectors, and the discrepancy between its RF-based and partitioned NEE estimates is the smallest of all eight sectors (Sect. 4.3). This grassland sink strength compares favourably with other managed, humid or grazed temperate grasslands (Table 4; Jaksic et al., 2006; Senapati et al., 2014), though it should still be interpreted with some residual caution given its position adjacent to the drainage network.

By contrast, the carbon budgets derived for the mixed-grain (Sector 2, NEE = +151 gC m^{-2} yr^{-1}) and hybrid transition zone (Sector 1, NEE = +195 gC m^{-2} yr^{-1}) sectors should be interpreted with considerably more caution. Given the site configuration — both sectors lie directly adjacent to the Brune ditch and/or its secondary branch and their riparian vegetation (Sect. 2.3.1, 3.3) — the corresponding NEE, GPP and Reco values cannot be considered fully representative of the mixed-grain crop, or of the grassland/mixed-grain transition, alone. The exceptionally high Reco recorded in Sector 1 (1700 gC m^{-2} yr^{-1}, the highest of the whole site; Sect. 4.3) most likely integrates a substantial riparian and/or ditch-adjacent respiratory signal rather than reflecting the transition vegetation alone. We therefore consider that, as constrained by a single EC tower, the mixed-grain carbon budget is not fully acceptable as a stand-alone, field-specific estimate, and recommend that it be interpreted qualitatively (net source behaviour, driven by a short and comparatively unproductive growing period followed by prolonged bare-soil respiration) rather than quantitatively; the hybrid-zone estimate should be treated with even greater caution, as a composite signal rather than a genuine parcel-specific budget (Sect. 3.3, 4.2, 4.3).

Comparing the four sectors together, the wheat and grassland carbon budgets, the two most robust estimates of this study, both point to net carbon sinks broadly consistent with other reported values for comparable crop and grassland systems (Table 4), whereas the mixed-grain and hybrid sectors, whose footprints are more exposed to riparian and ditch surfaces, both appear as net sources of comparable, moderate magnitude. A key factor underlying the contrast between the wheat/grassland and mixed-grain systems, beyond the footprint considerations above, is land-use history. The grassland and wheat plots have been under their respective management for many years, whereas the mixed grain was grassland before the measurement year and reverted

to grassland afterward (Guignard and Pouponnot, personal communications); the mixed-grain system was thus a one-off cereal rotation rather than an established crop. Crop-rotation studies indicate that continuous annual cropping tends to reduce productivity, and thus carbon uptake, relative to long-term rotations or perennial cover, owing to changes in soil structure, nutrient cycling and microbial communities (Liebman and Dyck, 1993), and biodiversity/rotation experiments have similarly shown that systems with longer-lived, diverse plant communities achieve greater and more stable productivity than single-year crops (Tilman et al., 2006).

The modest carbon uptake found in the mixed-grain sector in the present study is thus consistent with its transient status: the recent conversion from grassland is associated with lower soil organic matter quality and microbial carbon-use efficiency, which can reduce photosynthetic capacity while still sustaining substantial post-harvest soil respiration, as reported for short-term grassland-to-cropland conversions elsewhere (Mukumbuta et al., 2019).

The established winter wheat field, on the other hand, was almost neutral in full carbon accounting: once grain removal (≈ 250 gC m^{-2} via harvest) is taken into account, the sink behaviour reported here (Sects. 3.2, 3.4) would be largely offset. This agrees with other studies of long-term cereal monocultures (e.g. Schmidt et al., 2011) that find harvest removals can balance the high productivity of wheat. The hybrid sector (mixed-grain/grassland transition, riparian buffer) produced the largest net CO_2 source of the site; its amplified emissions arose from both the large respiration pulse of the mixed-grain crop after harvest and the continued respiration of the perennial grassland and riparian vegetation components integrated within its footprint (Sect. 4.3).

The present study solely focuses on NEE values and harvested biomass, without incorporating all carbon pathways, in particular stocks and associated changes in soil organic carbon and lateral hydrological fluxes, which are particularly important to draw a precise integrated carbon budget of the site. Simultaneous water pCO_2 measurements conducted in November 2023 within the LRTZC project indicated mean water CO_2 emissions of 12.42 ± 14.54 mmol m^{-2} h^{-1} (equivalent to approximately 3.45 ± 4.04 µmol m^{-2} s^{-1}, data not shown) from the ditch surface, which contrast with the cumulative NEE values obtained in the present study for the surrounding parcels; from previous bimonthly water carbon and discharge measurements carried out in 2017 and 2018 in the different watercourses of the Marais poitevin watershed flowing to the Aiguillon bay, an annual terrestrial carbon export of 15 gC m^{-2} yr^{-1} was estimated (Coignot et al., 2020). These carbon fluxes (i.e. water-air CO_2 flux and carbon export values) highlight the importance of lateral aquatic fluxes that need to be taken into account to draw the whole regional carbon budget of the land-sea continuum formed by the Marais poitevin wetland and the Aiguillon tidal bay (Polsenaere, 2025).

~~- Annual cumulative NEE estimates revealed clear contrasts among land uses. The permanently grazed grassland and winter wheat plots acted as strong net carbon sinks (−259 and −216 gC m^{-2} yr^{-1}, respectively), whereas the mixed-grain and hybrid systems were net carbon sources (+182 and +231 gC m^{-2} yr^{-1}). These values are broadly consistent with corresponding values from comparable crop sites elsewhere found the literature (Table 2). For example, managed humid grasslands have been reported with annual NEE values in the range of roughly −200 to −260 gC m^{-2} yr (Jaksic et al., 2006), and mowed or grazed grasslands often show high seasonal uptake, for instance,e.g. Senapati et al. (2014) reported −476 gC m^{-2} yr^{-1} for a mowed~~

grassland and -231 gC m^{-2} yr^{-1} for a grazed grassland. Winter wheat sink strength is also in line with other reported values;; for instance, Schmidt et al. (2012) found ~−270 gC m^{-2} yr^{-1} for winter wheat, through two years of EC measurements.

A key factor underlying these site differences is land use history. The grassland and wheat plots have been under their respective management for many years, whereas the mixed grain was grassland before measurements year and reverted to grassland afterward (Guignard and Pouponnot, personal communications). Indeed, the mixed grain system was a one-off cereal rotation rather than an established crop. Crop rotation studies indicate that continuous annual cropping tends to reduce productivity (and thus carbon uptake) relative to long-term rotations or perennial cover, due to changes in soil structure, nutrient cycling and microbial communities (Liebman and Dyck, 1993). Similarly, biodiversity and rotation experiments have shown that systems with longer-lived, diverse plant communities achieve greater and more stable productivity than single-year crops (Tilman et al., 2006). Then, the modest uptake in the mixed grain sector found in the present study likely reflects its transient status: the recent conversion from grassland meant lower soil organic matter quality and microbial efficiency, reducing photosynthetic carbon uptake, while still allowing substantial post-harvest soil respiration.

By contrast, the established winter wheat field was almost neutral in full carbon accountingBy contrast, the established winter wheat field behaved almost neutrally in full carbon accounting; indeed,. oOnce grain removal (~ 250 gC m^{-2} via harvest) is considered, our the high measured sink behaviour as observed in the present study would be largely offset. This agrees with other studies of long-term cereal monocultures (e.g. Schmidt et al. 2011), which that find that harvest removals can balance the high productivity of wheat. The hybrid system (cereal crop plus adjacent grazed grassland) produced the largest net CO_2 source;. iIts amplified emissions arose from both the large respiration pulse of the mixed grain crop after harvest and the continued nighttime respiration of the perennial grassland component.

The budgets present studyed solely here focuses solely on atmospheric NEE values and harvested biomass, without incorporating all carbon pathways, in particular, stocks and associated changes in soil organic carbon and lateral hydrological fluxes particularly important to draw a precise integrated carbon budget of the site. Simultaneous water pCO_2 measurements conducted in November 2023 within the LRTZC project indicated mean water CO_2 emissions of 12.42 ± 14.54 mmol m^{-2} h^{-1} (equivalent to approximately 3.45 ± 4.04 µmol m^{-2} s^{-1}, data not shown) from the ditch surface that contrast in comparison with cumulativeed NEE values obtained in the present study; from previous bimonthly water carbon and discharge measurements carried out in 2017 and 2018 in the different watercourses of the Marais poitevin watershed flowing to the Aiguillon bay, an annual terrestrial carbon export of 15 gC m^{-2} yr^{-1} was estimated (Coignot et al., 2020). These carbon fluxes (i.e. water-air CO_2 flux and carbon export values) highlight the importance of lateral aquatic fluxes that need to be taken into account to draw the whole regional carbon budget of the land-sea continuum formed by the Marais poitevin wetland and the Aiguillon tidal bay (Polsenaere, 2025); Polsenaere et al., in prep.).

Table 42. Annual net ecosystem exchange (NEE, in gC m^{-2} yr^{-1}) values found from this study and comparable literature. Site information and methodology are specified. Negative values indicate net CO_2 uptake (sink). See text for details of site conditions.

Reference (Location)	Vegetation/Crop	Method	Annual NEE (gC m^{-2} yr^{-1})	Notes
Jaksic et al. 2006 (Ireland)	Managed humid grassland	EC (2 years)	-193 (wet year); -258 (dry)	No moisture stress (soil > wilting point)
Senapati et al. 2014 (France)	Sown grassland (mowed)	EC (1 yr)	-476	"Mowing" management; net C storage ~+23 gC (after harvest)
Senapati et al. 2014 (France)	Sown grassland (grazed)	EC (1 yr)	-231	"Grazing" management; net C storage ~+141 gC
Wang et al., 2013 (China)	Winter wheat (crop season)	EC & auto-chamber	-251 (EC, seasonal)	Chamber EC comparison; EC flux matched AC flux within 7%
Schmidt et al. 2012 (Germany)	Winter wheat (annual)	EC (2 yrs)	-270 (Yr1); -270 (Yr2)	High uptake: field was a net source if harvest C removed
This study (France)	Permanent grassland~~Temperate grassland~~	EC + RF model	-145~~259~~	Sector 8; permanent grazed grassland; measured 2023-2024~~Permanent grass; measured 2023~~
This study (France)	Winter wheat	EC + RF model	-308~~216~~	Sectors 4+5+6 combined; harvested 7 July 2023~~Residues removed post-harvest; measured 2023~~
This study (France)	Mixed grain	EC + RF model	+151~~182~~	Sector 2; one-off rotation, ex-grassland; harvested 24 May 2023; footprint partly exposed to ditch~~Similar management to wheat, lower growth~~
This study (France)	Hybrid grassland/mixed-grain transition~~Hybrid cereal/grass mix~~	EC + RF model	+195~~231~~	Sector 1; composite signal incl. riparian vegetation; highest Reco of all sectors~~Intercropped cereals in riparian buffer~~

~~The combined EC-RF framework demonstrates that a single-tower, sector-partitioned approach can yield robust field-scale NEE estimates suitable for integration into regional or national greenhouse gas inventories, particularly in heterogeneous wetland-agricultural environments. By attributing fluxes to discrete land covers, this method bridges the gap between plot-~~

~~level process studies and coarser ecosystem models or remote-sensing products. Nonetheless, direct application at larger scales requires caution: the flux footprint can expand under stable conditions or complex terrain, and one-year dataset may not capture interannual variability in crop rotations or extreme weather. Moreover, by focusing on atmospheric NEE, other carbon budget components (soil carbon changes, dissolved carbon losses, biomass exports) are omitted. Without coordinated soil sampling, stream water monitoring and harvest accounting, full budget closure is not achieved. The reliability of the RF gap-filling also depends on high-quality, representative training data; noisy measurement periods (e.g. storm-induced artifacts) degrade model performance, and models trained under one regime may not generalize without retraining.~~

~~Future efforts should address these limitations by integrating dynamic footprint modelling, extending monitoring across crop rotations and climate gradients, and including complementary soil and aquatic measurements. Such efforts would enable truly field-resolved carbon budgets that capture all relevant pathways and inform both scientific understanding and policy decisions.~~

5 Conclusions

This study shows that a single, cost-effective Eddy Covariance tower, combined with wind-sector partitioning and sector-specific Random Forest modelling, can resolve contrasting annual NEE dynamics across a heterogeneous agricultural mosaic without multiple flux towers. While a pooled, sector-agnostic model matched the sector-specific models in point-prediction performance, it strongly compressed, and in one case inverted, the inter-sector contrasts once fluxes were reconstructed over the full year — a shrinkage effect toward the dominant sector's response that makes the sector-specific approach a necessary, not merely preferable, choice for such heterogeneous sites. Partitioning the fluxes into GPP and Reco confirmed these results and showed that sectors with similar land-cover labels can still have markedly different carbon dynamics.

Over the study year, the permanent grassland and the winter wheat field acted as net carbon sinks (−145 and −308 gC m^{-2} yr^{-1}), while the mixed-grain field acted as net source (+151 gC m^{-2} yr^{-1}). These estimates are not equally reliable: the wheat and grassland budgets are well constrained, whereas the mixed-grain sectors, adjacent to drainage ditches and riparian vegetation, yield more composite, cautiously-interpreted estimate. Key limitations include the one-year observation period and the exclusion of soil carbon and lateral aquatic fluxes from the budget. Beyond these limitations, this single-tower, wind-sector framework offers a transferable, low-cost alternative to multi-tower setups for resolving field-scale carbon dynamics in other heterogeneous agricultural landscapes.

Appendix A

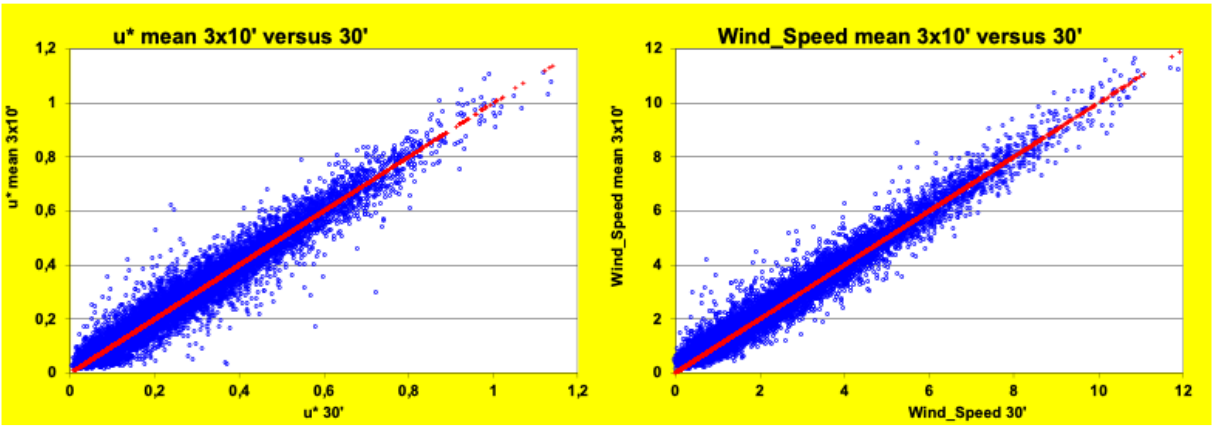


Figure A1. Friction velocity (u^*) and wind speed data as the mean of the three 10 min. values versus corresponding mean values obtained with an averaging time period of 30 min. (Comparisons done between 10 min. and 30 min. data showed that, according to the land parcel, a loose between 21% (wheat, sector 213°-283° with dominant wind directions) and 49% (wheat, sector 133°-173°) of data would be obtained with a choice of 30 min. mean flux calculation instead of the 10 min. mean flux procedure used here)

Appendix B

Table B1. Random Forest model parametrization.

Parameter	Value description
Algorithm	Random Forest regression (R~~r~~andomForest package, R)
Number of trees (ntree)	300
Number of variables tried at each split (mtry)	⌊√(number of predictors)⌋ = ⌊√8⌋ = 2
Node/leaf size	Default ~~randomForest~~RF settings (not modified)
Predictor variables (8)	PAR, relative humidity, air temperature, wind direction, day of year (DOY), soil moisture, soil temperature, day/night category (PAR > 10)
Target variable	Filtered NEE (CO_2 flux after hard-limit/QA filtering)
Uncertainty estimation	Bootstrap aggregation, B = 100 resamples (sampling with replacement) per sector/period model
Ensemble prediction	Median of the 100 bootstrap RF predictions

95% prediction interval	2.5th–97.5th percentile of the 100 bootstrap predictions
Performance metrics	RMSE, MAE, R^2 (computed between observed flux and bootstrap-median prediction)

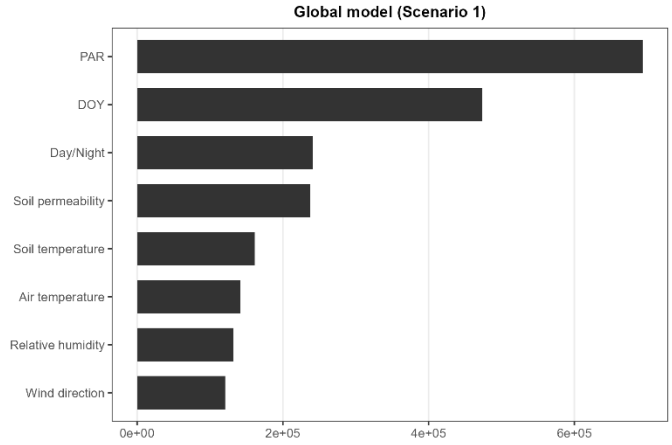


Figure B~~A~~21. Variable importance of the global model (Scenario 1), expressed as percentage increase in mean squared error (%IncMSE)

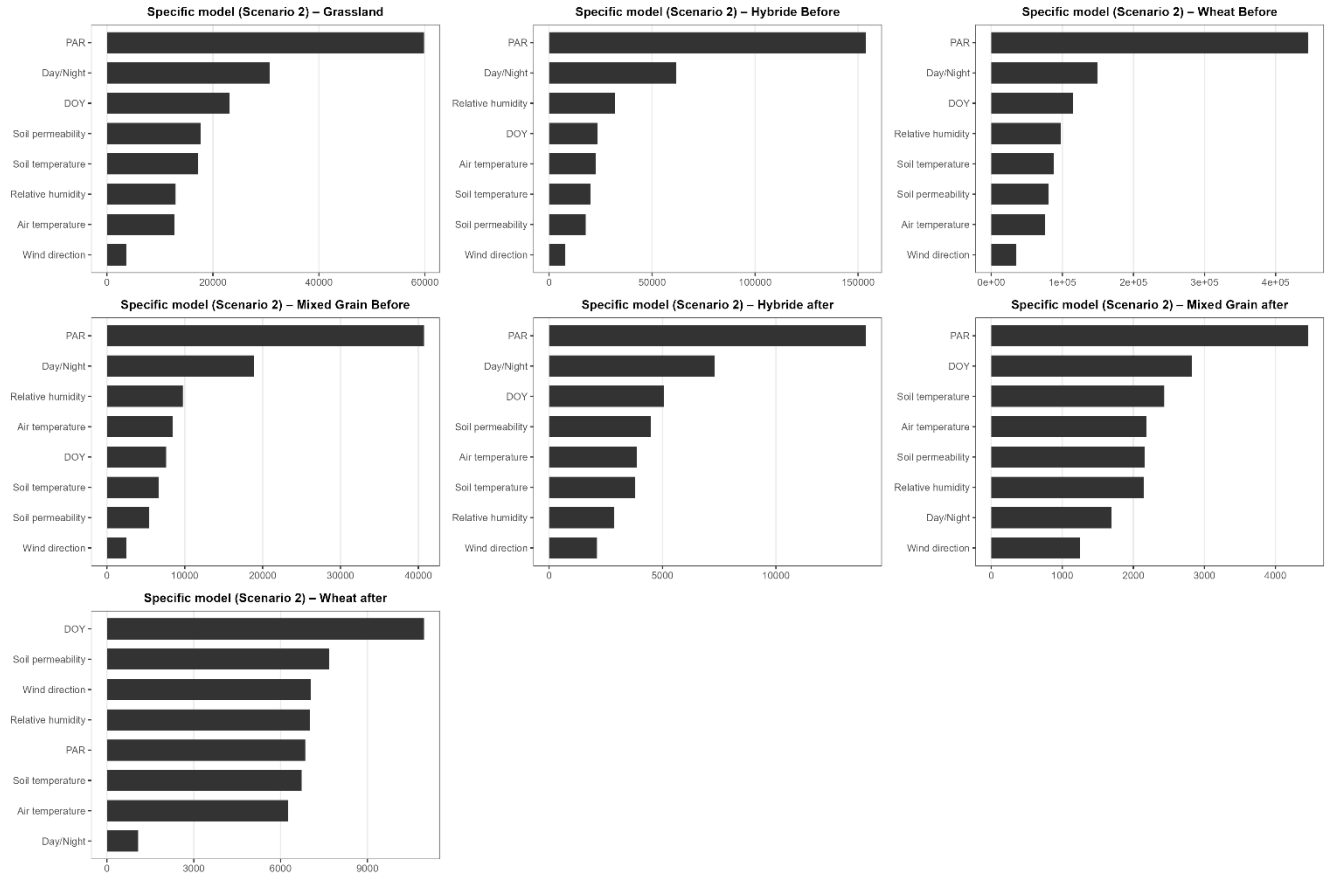


Figure ~~BA~~32. Variable importance across individual models in Scenario 2, expressed as percentage increase in mean squared error (%IncMSE)

Code/Data availability

All raw data can be provided by the corresponding authors upon request.

Author contribution

PP, EL, CP designed the study. PP, CD obtained the funding. PP, CP, JD performed the field work (EC tower deployment, maintenance, data retrieval). CP, PP, EL investigated and processed the data. PP, EL, NV, SB provided resources for data analysis. CP, PP, EL, NV, VM validated the data. CP made the graphics, wrote the draft. CP, PP led the review process assisted by CD, NV, OP.

Competing interests

The authors declare that they have no conflict of interest.

Acknowledgements

This work is a contribution of Camille Pery's two years work-study contract at Ifremer (Sept. 2022-Sept. 2024) in relationships with the LRTZC project (2019-2027: *La Rochelle Territoire Zero Carbone,* PIA TIGA #25875420; Caisse des Dépôts, Région Nouvelle-Aquitaine) and related to the ANR-22-PEXF-0006 - CarboNium project. We are grateful to our Ifremer colleague Louis Costes for his help in setting up the EC station, and to Wilfried Guignard and Rodolphe Pouponnot for the culture (management) information they provided us. We thank Maxime Paschal for his work on NDVI data during his internship and Nicolas Lachaussée for organizing drone flights.

References

Agreste: Mémento de la statistique agricole – Nouvelle-Aquitaine, Ministère de l'Agriculture et de la Souveraineté alimentaire, DRAAF Nouvelle-Aquitaine, 2020.

Bajgain, R., Xiao, X., Basara, J., Wagle, P., Zhou, Y., Mahan, H., Gowda, P., McCarthy, H. R., Northup, B., Neel, J., and Steiner, J.: Carbon dioxide and water vapor fluxes in winter wheat and tallgrass prairie in central Oklahoma, Sci. Total Environ., 644, 1511–1524, https://doi.org/10.1016/j.scitotenv.2018.07.010, 2018.

Baldocchi, D. D.: How eddy covariance flux measurements have contributed to our understanding of Global Change Biology, Glob. Change Biol., 26, 242–260, https://doi.org/10.1111/gcb.14807, 2020.

Barr, A. G., Richardson, A. D., Hollinger, D. Y., Papale, D., Arain, M. A., Black, T. A., Bohrer, G., Dragoni, D., Fischer, M. L., Gu, L., Law, B. E., Margolis, H. A., McCaughey, J. H., Munger, J. W., Oechel, W., and Schaeffer, K.: Use of change-point detection for friction–velocity threshold evaluation in eddy-covariance studies, Agric. For. Meteorol., 171–172, 31–45, https://doi.org/10.1016/j.agrformet.2012.11.023, 2013.

Bolsée, S., Dupont, S., Lamaud, E., Irvine, M., Lafont, S., Chipeaux, C., Garrigou, C., Bonnefond, J.M., Domec, J.C., Loustau, D. : Wind flow dynamics over a photovoltaic power plant: comparison with a vegetated canopy, in preparation, 2026

Bou-Zeid, E., Anderson, W., Katul, G. G., and Mahrt, L.: The Persistent Challenge of Surface Heterogeneity in Boundary-Layer Meteorology: A Review, Bound.-Layer Meteorol., 177, 227–245, https://doi.org/10.1007/s10546-020-00551-8, 2020.

Breiman, L.: Random Forests, Mach. Learn., 45, 5–32, https://doi.org/10.1023/A:1010933404324, 2001.

Burba, G.: Eddy Covariance Method for Scientific, Industrial, Agricultural and Regulatory Applications: A Field Book on Measuring Ecosystem Gas Exchange and Areal Emission Rates, https://doi.org/10.13140/RG.2.1.4247.8561, 2013.

Butzer, K. W.: French Wetland Agriculture in Atlantic Canada and Its European Roots: Different Avenues to Historical Diffusion, Ann. Assoc. Am. Geogr., 92, 451–470, https://doi.org/10.1111/1467-8306.00299, 2002.

Callejas-Rodelas, J. Á., Knohl, A., Mammarella, I., Vesala, T., Peltola, O., and Markwitz, C.: Does increased spatial replication above heterogeneous agroforestry improve the representativeness of eddy covariance measurements?, Biogeosciences, 22, 4507–4529, https://doi.org/10.5194/bg-22-4507-2025, 2025.

Chen, B., Coops, N. C., Fu, D., Margolis, H. A., Amiro, B. D., Barr, A. G., Black, T. A., Arain, M. A., Bourque, C. P.-A., Flanagan, L. B., Lafleur, P. M., McCaughey, J. H., and Wofsy, S. C.: Assessing eddy-covariance flux tower location bias across the Fluxnet-Canada research network based on remote sensing and footprint modelling, Agric. For. Meteorol., 151, 87–100, https://doi.org/10.1016/j.agrformet.2010.09.005, 2011.

Chu, H., Baldocchi, D. D., Poindexter, C., Abraha, M., Desai, A. R., Bohrer, G., Arain, M. A., Griffis, T., Blanken, P. D., O'Halloran, T. L., Thomas, R. Q., Zhang, Q., Burns, S. P., Frank, J. M., Christian, D., Brown, S., Black, T. A., Gough, C. M., Law, B. E., Lee, X., Chen, J., Reed, D. E., Massman, W. J., Clark, K., Hatfield, J., Prueger, J., Bracho, R., Baker, J. M., and Martin, T. A.: Temporal dynamics of aerodynamic canopy height derived from eddy covariance momentum flux data across North American flux networks, Geophys. Res. Lett., 45, 9275–9287, https://doi.org/10.1029/2018GL079306, 2018.

Coignot, E., Polsenaere, P., Soletchnik, P., Le Moine, O., Souchu, P., Joyeux, E., Le Roy, Y., Guéret, J.-P., Froud, L., Gallais, R., Chourré, E., Chaigneau, L., Soletchnik, P., Le Moine, O., Souchu, P., Joyeux, E., Le Roy, Y., Guéret, J.-P., Froud, L., Gallais, R., Chourré, E., and Chaigneau, L.: Variabilité spatio-temporelle des nutriments et du carbone et flux associés le long d'un continuum terrestre-aquatique tempéré (Marais poitevin – Baie de l'Aiguillon – Pertuis Breton), 2020.

Cunliffe, A. M., Boschetti, F., Clement, R., Sitch, S., Anderson, K., Duman, T., Zhu, S., Schlumpf, M., Litvak, M. E., Brazier, R. E., and Hill, T. C.: Strong correspondence in evapotranspiration and carbon dioxide fluxes between different eddy covariance systems enables quantification of landscape heterogeneity in dryland fluxes, J. Geophys. Res.-Biogeosciences, 127, e2021JG006240, https://doi.org/10.1029/2021JG006240, 2022

Flanagan, L. B. and Adkinson, A. C.: Interacting controls on productivity in a northern Great Plains grassland and implications for response to ENSO events, Glob. Change Biol., 17, 3293–3311, https://doi.org/10.1111/j.1365-2486.2011.02461.x, 2011.

Friedlingstein, P., O'Sullivan, M., Jones, M. W., Andrew, R. M., Hauck, J., Landschützer, P., Le Quéré, C., Li, H., Luijkx, I. T., Olsen, A., Peters, G. P., Peters, W., Pongratz, J., Schwingshackl, C., Sitch, S., Canadell, J. G., Ciais, P., Jackson, R. B., Alin, S. R., Arneth, A., Arora, V., Bates, N. R., Becker, M., Bellouin, N., Berghoff, C. F., Bittig, H. C., Bopp, L., Cadule, P., Campbell, K., Chamberlain, M. A., Chandra, N., Chevallier, F., Chini, L. P., Colligan, T., Decayeux, J., Djeutchouang, L. M., Dou, X., Duran Rojas, C., Enyo, K., Evans, W., Fay, A. R., Feely, R. A., Ford, D. J., Foster, A., Gasser, T., Gehlen, M., Gkritzalis, T., Grassi, G., Gregor, L., Gruber, N., Gürses, Ö., Harris, I., Hefner, M., Heinke, J., Hurtt, G. C., Iida, Y., Ilyina, T., Jacobson, A. R., Jain, A. K., Jarníková, T., Jersild, A., Jiang, F., Jin, Z., Kato, E., Keeling, R. F., Klein Goldewijk, K., Knauer, J., Korsbakken, J. I., Lan, X., Lauvset, S. K., Lefèvre, N., Liu, Z., Liu, J., Ma, L., Maksyutov, S., Marland, G., Mayot, N., McGuire, P. C., Metzl, N., Monacci, N. M., Morgan, E. J., Nakaoka, S.-I., Neill, C., Niwa, Y., Nützel, T., Olivier, L., Ono, T., Palmer, P. I., Pierrot, D., Qin, Z., Resplandy, L., Roobaert, A., Rosan, T. M., Rödenbeck, C., Schwinger, J., Smallman, T. L., Smith, S. M., Sospedra-Alfonso, R., Steinhoff, T., et al.: Global Carbon Budget 2024, Earth Syst. Sci. Data, 17, 965–1039, https://doi.org/10.5194/essd-17-965-2025, 2025.

Gao, D., Yao, J., Yu, S., Ma, Y., Li, L., and Gao, Z.: Eddy Covariance CO2 Flux Gap Filling for Long Data Gaps: A Novel Framework Based on Machine Learning and Time Series Decomposition, Remote Sens., 15, 2695, https://doi.org/10.3390/rs15102695, 2023.

Gash, J. H. C. and Culf, A. D.: Applying a linear detrend to eddy correlation data in realtime, Bound.-Layer Meteorol., 79, 301–306, https://doi.org/10.1007/BF00119443, 1996.

Genuer, R., Poggi, J.-M., and Tuleau-Malot, C.: Variable selection using random forests, Pattern Recognit. Lett., 31, 2225–2236, https://doi.org/10.1016/j.patrec.2010.03.014, 2010.

Gilmanov, T. G., Verma, S. B., Sims, P. L., Meyers, T. P., Bradford, J. A., Burba, G. G., and Suyker, A. E.: Gross primary production and light response parameters of four Southern Plains ecosystems estimated using long-term CO2-flux tower measurements, Glob. Biogeochem. Cycles, 17, undefined-undefined, https://doi.org/10.1029/2002gb002023, 2003.

Gu, L., Falge, E. M., Boden, T., Baldocchi, D. D., Black, T. A., Saleska, S. R., Suni, T., Verma, S. B., Vesala, T., Wofsy, S. C., and Xu, L.: Objective threshold determination for nighttime eddy flux filtering, Agric. For. Meteorol., 128, 179–197, https://doi.org/10.1016/j.agrformet.2004.11.006, 2005.

Heimsch, L., Lohila, A., Tuovinen, J.-P., Vekuri, H., Heinonsalo, J., Nevalainen, O., Korkiakoski, M., Liski, J., Laurila, T., and Kulmala, L.: Carbon dioxide fluxes and carbon balance of an agricultural grassland in southern Finland, Biogeosciences, 18, 3467–3483, https://doi.org/10.5194/bg-18-3467-2021, 2021.

Hernandez Rodriguez, L. C., Goodwell, A. E., and Kumar, P.: Inside the flux footprint: The role of organized land cover heterogeneity on the dynamics of observed land-atmosphere exchange fluxes, Front. Water, 5, https://doi.org/10.3389/frwa.2023.1033973, 2023.

Jaksic, V., Kiely, G., Albertson, J., Oren, R., Katul, G., Leahy, P., and Byrne, K. A.: Net ecosystem exchange of grassland in contrasting wet and dry years, Agric. For. Meteorol., 139, 323–334, https://doi.org/10.1016/j.agrformet.2006.07.009, 2006.

Kirschbaum, M. U. F.: The temperature dependence of soil organic matter decomposition, and the effect of global warming on soil organic C storage, Soil Biol. Biochem., 27, 753–760, https://doi.org/10.1016/0038-0717(94)00242-S, 1995.

Kljun, N., Calanca, P., Rotach, M. W., and Schmid, H. P.: A simple parameterisation for flux footprint predictions, Bound.-Layer Meteorol., 112, 503–523, https://doi.org/10.1023/B:BOUN.0000030653.71031.96, 2004.

Kljun, N., Calanca, P., Rotach, M. W., and Schmid, H. P.: A simple two-dimensional parameterisation for Flux Footprint Prediction (FFP), Geosci. Model Dev., 8, 3695–3713, https://doi.org/10.5194/gmd-8-3695-2015, 2015.

Knauer, J., Zaehle, S., Medlyn, B. E., Reichstein, M., Williams, C. A., Migliavacca, M., De Kauwe, M. G., Werner, C., Keitel, C., Kolari, P., Limousin, J.-M., and Linderson, M.-L.: Towards physiologically meaningful water-use efficiency estimates from eddy covariance data, Glob. Change Biol., 24, 694–710, https://doi.org/10.1111/gcb.13893, 2018.

Kowalski, S., Sartore, M., Burlett, R., Berbigier, P., and Loustau, D.: The annual carbon budget of a French pine forest (Pinus pinaster) following harvest, Glob. Change Biol., 9, 1051–1065, https://doi.org/10.1046/j.1365-2486.2003.00627.x, 2003.

Kowalski, A. S., Loustau, D., Berbigier, P., Manca, G., Tedeschi, V., Borghetti, M., Valentini, R., Kolari, P., Berninger, F., Rannik, Ü., Hari, P., Rayment, M., Mencuccini, M., Moncrieff, J., and Grace, J.: Paired comparison of carbon exchange between undisturbed and regenerating stands in four managed forests in Europe, Glob. Change Biol., 10, 1707–1723, https://doi.org/10.1111/j.1365-2486.2004.00846.x, 2004.

Kumari, S., Kambhammettu, B. V. N. P., and Niyogi, D.: Sensitivity of Analytical Flux Footprint Models in Diverse Source-Receptor Configurations: A Field Experimental Study, J. Geophys. Res. Biogeosciences, 125, e2020JG005694, https://doi.org/10.1029/2020JG005694, 2020.

Liebman, M. and Dyck, E.: Crop Rotation and Intercropping Strategies for Weed Management, Ecol. Appl., 3, 92–122, https://doi.org/10.2307/1941795, 1993.

Liu, L., Zhou, W., Guan, K., Peng, B., Xu, S., Tang, J., Zhu, Q., Till, J., Jia, X., Jiang, C., Wang, S., Qin, Z., Kong, H., Grant, R., Mezbahuddin, S., Kumar, V., and Jin, Z.: Knowledge-guided machine learning can improve carbon cycle quantification in agroecosystems, Nat. Commun., 15, 357, https://doi.org/10.1038/s41467-023-43860-5, 2024.

Lloyd, J. and Taylor, J. A.: On the Temperature Dependence of Soil Respiration, Funct. Ecol., 8, 315–323, https://doi.org/10.2307/2389824, 1994.

Mahecha, M. D., Reichstein, M., Carvalhais, N., Lasslop, G., Lange, H., Seneviratne, S. I., Vargas, R., Ammann, C., Arain, M. A., Cescatti, A., Janssens, I. A., Migliavacca, M., Montagnani, L., and Richardson, A. D.: Global Convergence in the Temperature Sensitivity of Respiration at Ecosystem Level, Science, 329, 838–840, https://doi.org/10.1126/science.1189587, 2010.

Mayen, J., Polsenaere, P., Lamaud, É., Arnaud, M., Kostyrka, P., Bonnefond, J.-M., Geairon, P., Gernigon, J., Chassagne, R., Lacoue-Labarthe, T., Regaudie de Gioux, A., and Souchu, P.: Atmospheric CO_2 exchanges measured by eddy covariance over a temperate salt marsh and influence of environmental controlling factors, Biogeosciences, 21, 993–1016, https://doi.org/10.5194/bg-21-993-2024, 2024.

Mayen, J., Polsenaere, P., Regaudie de Gioux, A., Deborde, J., Collin, K., Le Merrer, Y., Foucault, É., Ouisse, V., André, L., Arnaud, M., Kostyrka, P., Lamaud, É., Abril, G., and Souchu, P.: Aquatic metabolism influences temporal variations of water carbon and atmospheric carbon dioxide fluxes in a temperate salt marsh, Biogeosciences, 22, 5387–5411, https://doi.org/10.5194/bg-22-5387-2025, 2025.

Moreaux, V., Longdoz, B., Berveiller, D., Delpierre, N., Dufrêne, E., Bonnefond, J.-M., Chipeaux, C., Joffre, R., Limousin, J.-M., Ourcival, J.-M., Klumpp, K., Darsonville, O., Brut, A., Tallec, T., Ceschia, E., Panthou, G., and Loustau, D.: Environmental control of land-atmosphere CO2 fluxes from temperate ecosystems: a statistical approach based on homogenized time series from five land-use types, Tellus B Chem. Phys. Meteorol., 72, 2020.

Mukumbuta, I., Shimizu, M., and Hatano, R.: Short-term land-use change from grassland to cornfield increases soil organic carbon and reduces total soil respiration, Soil Tillage Res., 186, 1–10, 2019.

Novick, K. A., Ficklin, D. L., Stoy, P. C., Williams, C. A., Bohrer, G., Oishi, A. C., Papuga, S. A., Blanken, P. D., Noormets, A., Sulman, B. N., Scott, R. L., Wang, L., and Phillips, R. P.: The increasing importance of atmospheric demand for ecosystem water and carbon fluxes, Nat. Clim. Change, 6, 1023–1027, https://doi.org/10.1038/nclimate3114, 2016.

Oren, R., Hsieh, C.-I., Stoy, P., Albertson, J., McCarthy, H. R., Harrell, P., and Katul, G. G.: Estimating the uncertainty in annual net ecosystem carbon exchange: spatial variation in turbulent fluxes and sampling errors in eddy-covariance measurements, Glob. Change Biol., 12, 883–896, https://doi.org/10.1111/j.1365-2486.2006.01131.x, 2006.

Papale, D., Reichstein, M., Aubinet, M., Canfora, E., Bernhofer, C., Kutsch, W., Longdoz, B., Rambal, S., Valentini, R., Vesala, T., and Yakir, D.: Towards a standardized processing of Net Ecosystem Exchange measured with eddy covariance technique: algorithms and uncertainty estimation, Biogeosciences, 3, 571–583, https://doi.org/10.5194/bg-3-571-2006, 2006.

Polsenaere, P., Lamaud, E., Lafon, V., Bonnefond, J.-M., Bretel, P., Delille, B., Deborde, J., Loustau, D. and Abril, G.: Spatial and temporal CO2 exchanges measured by Eddy Covariance over a temperate intertidal flat and their relationships to net ecosystem production, Biogeosciences, 9, 249–268, https://doi.org/10.5194/bg-9-249-2012, 2012.

Polsenaere, P.: Dynamique du carbone en zone côtière tempérée: processus biogéochimiques et échanges aux interfaces terre – zone côtière – atmosphère. HDR. https://archimer.ifremer.fr/doc/00993/110419/, 2025.

Rannik, Ü., Mammarella, I., Vesala, T., Väkimies, P., Heiskari-Tuohiniemi, H., and Korkiakoski, M.: Good performance of low-cost carbon dioxide sensor based on intercomparisons with the standard eddy-covariance system, EGUsphere [preprint], https://doi.org/10.5194/egusphere-2026-144, 2026.

van Ramshorst, J. G. V., Knohl, A., Callejas-Rodelas, J. Á., Clement, R., Hill, T. C., Siebicke, L., and Markwitz, C.: Lower cost eddy covariance for CO2 and H2O fluxes over grassland and agroforestry, Atmos. Meas. Tech., 17, 6047–6071, https://doi.org/10.5194/amt-17-6047-2024, 2024.

Reichstein, M., Ciais, P., Papale, D., Valentini, R., Running, S., Viovy, N., Cramer, W., Granier, A., Ogée, J., Allard, V., Aubinet, M., Bernhofer, Chr., Buchmann, N., Carrara, A., Grünwald, T., Heimann, M., Heinesch, B., Knohl, A., Kutsch, W., Loustau, D., Manca, G., Matteucci, G., Miglietta, F., Ourcival, J. m., Pilegaard, K., Pumpanen, J., Rambal, S., Schaphoff, S., Seufert, G., Soussana, J.-F., Sanz, M.-J., Vesala, T., and Zhao, M.: Reduction of ecosystem productivity and respiration during the European summer 2003 climate anomaly: a joint flux tower, remote sensing and modelling analysis, Glob. Change Biol., 13, 634–651, https://doi.org/10.1111/j.1365-2486.2006.01224.x, 2007.

Reynolds: I. On the theory of lubrication and its application to Mr. Beauchamp tower's experiments, including an experimental determination of the viscosity of olive oil, Proc. R. Soc. Lond., 40, 191–203, https://doi.org/10.1098/rspl.1886.0021, 1886.

Schmidt, M., Reichenau, T. G., Fiener, P., and Schneider, K.: The carbon budget of a winter wheat field: An eddy covariance analysis of seasonal and inter-annual variability, Agric. For. Meteorol., 165, 114–126, https://doi.org/10.1016/j.agrformet.2012.05.012, 2012.

Schmidt, M. W. I., Torn, M. S., Abiven, S., Dittmar, T., Guggenberger, G., Janssens, I. A., Kleber, M., Kögel-Knabner, I., Lehmann, J., Manning, D. A. C., Nannipieri, P., Rasse, D. P., Weiner, S., and Trumbore, S. E.: Persistence of soil organic matter as an ecosystem property, Nature, 478, 49–56, https://doi.org/10.1038/nature10386, 2011.

Senapati, N., Chabbi, A., Gastal, F., Smith, P., Mascher, N., Loubet, B., Cellier, P., and Naisse, C.: Net carbon storage measured in a mowed and grazed temperate sown grassland shows potential for carbon sequestration under grazed system, Carbon Manag., 5, 131, https://doi.org/10.1080/17583004.2014.912863, 2014.

Tilman, D., Reich, P. B., and Knops, J. M. H.: Biodiversity and ecosystem stability in a decade-long grassland experiment, Nature, 441, 629–632, https://doi.org/10.1038/nature04742, 2006.

Vekuri, H., Tuovinen, J.-P., Kulmala, L., Papale, D., Kolari, P., Aurela, M., Laurila, T., Liski, J., and Lohila, A.: A Widely Used Eddy Covariance Gap-Filling Method Creates Systematic Bias in Carbon Balance Estimates, Scientific Reports, 13, 1720, https://doi.org/10.1038/s41598-023-28827-2, 2023.

Vickers, D. and Mahrt, L.: Quality Control and Flux Sampling Problems for Tower and Aircraft Data, 1997.

Wagle, P., Gowda, P. H., Northup, B. K., Turner, K. E., Neel, J. P. S., Manjunatha, P., and Zhou, Y.: Variability in carbon dioxide fluxes among six winter wheat paddocks managed under different tillage and grazing practices, Atmos. Environ., 185, 100–108, https://doi.org/10.1016/j.atmosenv.2018.05.003, 2018.

Wang, H., Jia, G., Zhang, A., and Miao, C.: Assessment of spatial representativeness of eddy covariance flux data from flux tower to regional grid, Remote Sens., 8, 742, https://doi.org/10.3390/rs8090742, 2016.

Wang, K., Liu, C., Zheng, X., Pihlatie, M., Li, B., Haapanala, S., Vesala, T., Liu, H., Wang, Y., Liu, G., and Hu, F.: Comparison between eddy covariance and automatic chamber techniques for measuring net ecosystem exchange of carbon dioxide in cotton and wheat fields, Biogeosciences, 10, 6865–6877, https://doi.org/10.5194/bg-10-6865-2013, 2013.

Wohlfahrt, G. and Gu, L.: The many meanings of gross photosynthesis and their implication for photosynthesis research from leaf to globe, Plant Cell Environ., 38, 2500–2507, https://doi.org/10.1111/pce.12569, 2015.

Wu, L., Miao, H., and Liu, T.: Development in Agricultural Ecosystems' Carbon Emissions Research: A Visual Analysis Using CiteSpace, Agronomy, 14, 1288, https://doi.org/10.3390/agronomy14061288, 2024.

Zeng, J., Matsunaga, T., Tan, Z.-H., Saigusa, N., Shirai, T., Tang, Y., Peng, S., and Fukuda, Y.: Global terrestrial carbon fluxes of 1999–2019 estimated by upscaling eddy covariance data with a random forest, Sci. Data, 7, 313, https://doi.org/10.1038/s41597-020-00653-5, 2020.

Zomer, R. J., Bossio, D. A., Sommer, R., and Verchot, L. V.: Global Sequestration Potential of Increased Organic Carbon in Cropland Soils, Sci. Rep., 7, 15554, https://doi.org/10.1038/s41598-017-15794-8, 2017.